Energy Conversion and Management 293 (2023) 117525

Contents lists available at ScienceDirect

Energy Conversion and Management

journal homepage: www.elsevier.com/locate/enconman

Catalyst-enhanced autothermal chemical looping reforming: Intrinsic SMR kinetics and numerical simulation

Zirui He [a,b,*,1], Florent Minette [a,b], Juray De Wilde [a,b,*]

[a] Université catholique de Louvain, Institute of Mechanics, Materials and Civil Engineering (iMMC) Materials & Process Engineering (IMAP), Place Sainte Barbe 2, B-1348 Louvain-la-Neuve, Belgium
[b] Research and Innovation Centre for Process Engineering (ReCIPE), Place Sainte Barbe 2, B-1348 Louvain-la-Neuve, Belgium

ARTICLE INFO

Keywords:
Chemical looping reforming
Catalysis
Steam methane reforming
Intrinsic kinetics
Fluidized bed modeling
Multi-scale modeling

ABSTRACT

In this work, we propose a catalyst-enhanced autothermal chemical looping reforming (CE-aCLR) to address the environmental concerns associated with toxic Ni-based oxygen carrier (OC) and the low fuel conversion related to the low reactivity of Fe-based OC. In this process, a non-toxic noble-metal-based steam methane reforming (SMR) catalyst is employed for methane conversion, while a Fe-based OC is employed for oxygen transfer between two reactors. Firstly, a commercial Rh-based SMR catalyst is studied in a micro-fixed bed reactor and its intrinsic reaction kinetics are determined. Then, a 1-D CE-aCLR model is developed based on a verified multi-scale aCLR model to facilitate analyzing commercial-scale feasibility. This model accounts for the essentials of the reactor hydrodynamics, mass and heat transfer, detailed reaction kinetics, and the influence of the solids residence time distribution in the fuel reactor. The main dimensions of a commercial CE-aCLR unit are determined and this unit is simulated using the developed model. The results demonstrate the feasibility of the novel, environmentally friendly process that enables high methane conversion using Fe-based OC within realistically sized reactors and an acceptable solid circulation rate. Moreover, sensitivity study shows that the CE-aCLR allows using OCs with low activity (potentially low cost) while maintaining high CH_4 conversion.

1. Introduction

Industrial development has resulted in a massive increase in greenhouse gas (GHG) emissions, which have caused climate change and more frequent and intense weather extremes [1]. Ihe IPCC has emphasized the need for immediate action to reduce GHG emissions, stating that "the time for action is now" in its latest report. CO_2 is the most prominent GHG, and its reduction requires action in every sector. Several CO_2 capture technologies have been developed at various stages of the energy conversion process, including oxyfuel combustion, calcium looping, integrated gasification combined cycle, and chemical looping [2,3].

Many industrial processes rely on the production of syngas and/or hydrogen through methane reforming, which is primarily derived from natural gas [4,5]. These processes include methanol production, Fischer-Tropsch (F-T) synthesis, and ammonia production [6–9]. The petrochemical, ammonia, and methanol industries account for roughly 90% of global hydrogen production, with 100% of the hydrogen used for ammonia production being produced by natural gas reforming [10,11]. Steam methane reforming (SMR) has been the dominant technology for methane conversion for several decades. Conventionally, SMR is carried out in tubular reactors (ca. 12 m long, 0.1 m in diameter) catalyzed by a Ni-based catalyst. Commercial scale SMR plants have hundreds of such reactor tubes suspended in a gas-fired furnace, which provides the heat for the endothermic methane reforming reactions [12–14]. Under the tightening environmental regulations, CO_2 capture is foreseen to be incorporated into SMR plants to reduce their CO_2 emissions, in particular from the furnace [10]. This is a challenging and costly undertaking Furthermore, heat transfer limitations from the furnace to the tubular reactors are known to determine the performance of SMR and to negatively impact their energy efficiency. Furthermore, the H_2-to-CO ratio of syngas produced from SMR is typically 3, while downstream processes such as F-T synthesis and methanol production require a ratio of around

* Corresponding authors at: Université catholique de Louvain, Institute of Mechanics, Materials and Civil Engineering (iMMC) Materials & Process Engineering (IMAP), Place Sainte Barbe 2, B-1348 Louvain-la-Neuve, Belgium.
E-mail addresses: zirui.he@foxmail.com (Z. He), juray.dewilde@uclouvain.be (J. De Wilde).
[1] Present address: School of Chemistry, Chemical Engineering and Biotechnology, Nanyang Technological University, 62 Nanyang Drive, Singapore 637459, Singapore.

https://doi.org/10.1016/j.enconman.2023.117525
Received 5 April 2023; Received in revised form 8 August 2023; Accepted 9 August 2023
Available online 16 August 2023

Nomenclature

Latin letters

a_v	Specific interface area per unit of reactor, [$m^2_{inteface}/m^3_r$]
$A(k_i/K_A)$	Pre-exponential factor of reaction rate constant or adsorption constant
Ar	Archimedes number, [-]
C^b_A, C^e_A, C^s_A	Concentration of gas species in bubble, emulsion phase and on catalyst surface, [mol_A/m^3_g]
C^k_i	Concentration of species i at k condition, see the meaning of the subscripts and superscripts, [mol_i/kg_{OC}] for solids and [mol_i/m^3_g] for gas
C_p	Specific heat of gas or solids, [kJ/kg·K]
d_t, d_p	Reactor diameter, and particle diameter [m]
DEN	Denominator in the rate equation of catalytic SMR reactions
$D_{AR/FR}$	Diameter of the AR/FR, [m]
D_{eg}, D_{es}	Effective diffusivity of gas/solids in emulsion phase [m^2_r/s]
D_i, $D_{0,i}$	Diffusivity in the rate equation of the reduction of FeOx by H_2, [m^2/s]
D_s	Diffusivity in the rate equation of the reduction of FeO by CO with the random pore model, [m^2/s]
E_{ai}	Activation energy of i reaction, [kJ/mol]
$E(t)$	Residence time distribution of solids in the FR, from step-response simulation of the FR using axial dispersion model, [-]
f_b, f_{eg}, f_{es}	Fraction of bubble, emulsion gas and solids in the bubbling fluidized bed reactor, [$m^3_{b/eg/s}/m^3_r$]
F^b_A, F^e_A	Flow rate of A species in bubbling or emulsion phase, [mol/m^2·s]
F_{O2}	Flow rate of O_2 in the AR, [mol/m^2·s]
g	Gravitational acceleration, [m/s^2]
G_g	Gas feeding rate, [kg/s]
h_i	the enthalpy of gas or solids species, [kJ/mol]
h_f	Heat transfer coefficient, [kJ/m^2·K·s]
$H_{AR/FR}$	Height of the AR/FR, [m]
k_I	Interexchange mass transfer coefficient between the bubble and emulsion phase, [m^3_g/m^2_r·s]
$k_{i,j}$	Kinetics constant of the reduction of i solids species with j gaseous species, see the meaning of the subscripts and superscripts
k_g	Gas-solid mass transfer coefficient, [$m^3_g/m^2_{inteface}$·s]
k_1, k_3	Kinetics constant of SMRI and SMRII reactions, [mol/kg_{cat}·s·$bar^{0.5}$]
k_2	Kinetics constant of WGS reaction, [mol/kg_{cat}·s·bar]
K_I, K_{III}	Reaction equilibrium constant of SMRI and SMRII reactions, [bar^2]
K_{II}	Reaction equilibrium constant of WGS reaction, [-]
K_{CH4}, K_{CO}, K_{H2}	Adsorption constant of CH_4, CO and H_2, [bar^{-1}]
K_{H2O}	Adsorption constant of H_2O, [-]
$K_{eq,i}$	Equilibrium constant of i reduction reaction, [-]
L_0	Length of the pore system per unit volume m^{-2} in rate equation of the reduction of FeO by CO, [m]
m^k_i	Molar flow of i species (can be gas and solids species) at k condition
$\dot{m}_s$	Solids circulation rate, [kg_s/s]
p	Pressure [bar]
p_A	Partial pressure of A (A = H_2, CH_4, H_2O, CO, CO_2), [bar]
p_{O2}	Partial pressure of O_2 on OC surface during oxidation, [bar]
r_0	Initial (average) grain radius, [m]
r_1, r_2, r_3	Reaction rate of SMRI, WGS and SMRII catalytic reactions, [mol_r/kg_{cat}·s]
r_{Fe}, r_{O2}	Fe and O_2 consuming rate in the AR, [mol_{Fe}/kg_{OC}·s], [mol_{O2}/kg_{OC}·s]
$r_{i,j,}$	Consumption rate of i solids species during the reduction of i solids species by j gaseous species, [mol_i/kg_{OC}·s]
$R^{SMR/Red}_A$	Overall reaction rate of A species in SMR or reduction reactions, [$mol_A/kg_{cat/OC}$·s]
R^{WGS}_A	Reaction rate to reach equilibrium of water gas shift, [mol_A/m^3_r·s]
R^{ave}_i	The volume-averaged reaction rate of i solids species with the mean reaction driving force accounting for the residence time distribution of particles in the FR, [mol_i/kg_{OC}·s]
$R_i(x^{ave}_i)$	The reaction rate of i solids species calculated with the mean reaction driving force and mean solids conversion, [mol_i/kg_{OC}·
Re	Reynold number [-]
S_0	initial specific surface area of inside a particle m^{-1} in rate equation of the reduction of FeO by CO [-]
s_{CO2},s_{CH4}	Selectivity to CO_2 in SMR tests and selectivity to CH_4 in methanation and reverse of water–gas-shift (RWGS) test
T_{m1}, T_{m2}	Mean temperature during methanation and RWGS and SMR test, [K]
u_{eg}	Emulsion gas flow rate, [m^3_{eg}/m^2_r·s]
u_{mf}, u_{sg}, u_t, u_{tr}	Minimum fluidization velocity, superficial gas velocity, terminal velocity and transport velocity, [m^3_g/m^2_r·s]
u_{sg}, u_{ss}	Superficial gas velocity and solids velocity, [$m^3_{g/s}/m^2_r$•s]
V_i	Approach-to-equilibrium of ith reaction, [-]
V_{FeO}	molar volume of wüstite, [m^3/mol]
W/F^0_{CH4}, W/F^0_{CO2}	Space time in SMR test and in methanation and RWGS test, [kg_{cat}•s/$mol_{CH4/CO2}$]
x_{CH4}, x_{CO2}	Conversion of CH_4 and conversion of CO_2, [-]
x_{Fe2O3}, x_{Fe3O4}, $x_{FeO,}$ x_{Fe}	Reduction conversion of Fe_2O_3, Fe_3O_4, FeO and Fe, [-]

Greek letters

α	Ratio of the molar volume of solid product to reactant in rate equation of the reduction of FeO by CO, [-]
α_{OC}	Fraction of oxygen carrier in the solid mixture, [kg_{OC}/kg_s]
α_{cat}	Fraction of SMR catalyst in the solid mixture, [kg_{cat}/kg_s]
β_i	Biot number in a random pore model of FeO reduction by CO, [-]
ε_0	Initial porosity of the particle in RPM of FeO reduction by CO, [-]
ε_g	Void in riser, [m^3_g/m^3_r]
η_s, η_g	Frictional factor in the riser for rate drop, see Supplementary Material.
μ	Gas viscosity, [kg/m·s]
ψ	Structural parameter in RPM of the FeO reduction by CO, [-]
$\rho_{OC/cat}$	Density of oxygen carrier and catalyst, [$kg_{OC/cat}/m^3_{OC/cat}$]
ρ^M_{Fe2O3}	Molar density of Fe_2O_3, [mol/m^3]
ϕ_{Red}	Effectiveness factor of reduction reactions due to particles residence time distribution, [-]
ΔH_{ai}	Adsorption heat of i species, [kJ/mol]
ΔH^0_r	Reaction enthalpy, [kJ/mol]
$\Delta F_{A,Ei}$	Excess flow from emulsion phase to bubble phase due to volume expansion, [mol_A/m^3_r·s]
Ω_r	Reactor surface area, [m^2]

Subscripts and superscripts

ave	Averaged
eqv	Equivalent
full ox	Full oxidation state
i	Solids species, Fe_2O_3, Fe_3O_4, FeO
in FR	At inlet of the FR
out AR	At AR outlet
out FR	At FR outlet

2 [15].

Autothermal Chemical Looping Reforming (aCLR) is seen as a promising technology that improves energy efficiency and facilitates CO_2 capture and utilization that has been actively studied in the past years [3,16,17]. Moreover, aCLR inherently produces syngas with a H_2-to-CO ratio close to 2 that is ideal for several downstream processes. Typically, aCLR system consists of an air reactor (AR) and a fuel reactor (FR) [17]. An oxygen carrier (OC), usually a metal oxide, is used to transport oxygen between the two reactors. The global reaction between methane and OC can be expressed as:

$$CH_4 + \frac{1}{y}MeO_x \rightarrow CO + 2H_2 + \frac{1}{y}MeO_{x-y}$$

After the OC being reduced, OC is transported to the AR and reacts with O_2:

$$MeO_{x-y} + \frac{y}{2}O_2 \rightarrow MeO_x$$

CLR has been demonstrated in various scales to investigate its feasibility [18]. For example, Rydén et al. [19] studied CLR in an interconnected fluidized bed reactor system using a NiO-$MgAl_2O_4$ OC. High syngas (CO and H_2) selectivity was achieved while coke formation was eliminated by co-feeding a small amount of steam (~25% of the CH_4). Diego et al. [20] studied CLR in a 900W_{th} circulating fluidized bed reactor under continuous operation. NiO on alumina was used as OC and a methane conversion higher than 98% was achieved under all operating conditions. Osman et al. [21] achieved autothermal operation of CLR in an internally circulated fluidized bed using NiO/Al_2O_3. At a larger scale, Pröll et al. [22] tested CLR in a 140kW_{th} interconnected fluidized bed system. Various feed stoichiometric air-to-CH_4 ratios, ca. 0.5–1.15, were tested while nearly full conversion of methane was achieved for all the cases. Fan et al. [23] demonstrated solid fuel based CLR in a 250kW_{th} moving bed reactor using an Fe-based OC. High fuel conversion was achieved with producing high purity H_2. Although several metals, including Ni, Fe, Cu, Mn, and Ce in their mono- or bi-metallic forms, have been investigated as active materials as OC for CLR [17,24–27], many OCs were not tested in real CLR operating conditions, but only tested in micro-fixed bed or TGA to evaluate their reduction and oxidation properties. Ni-based OCs have been extensively studied due to their high reactivity towards methane reforming [22,28,29]. However, the formation of cancerogenic Ni-containing dust during chemical looping processes presents a serious environmental concern, casting a shadow over the prospect of Ni-based OC for aCLR. Cu is another widely studied metal for chemical looping. The reactivity of Cu-based OCs is generally lower than that of Ni-based OCs but higher than that of Fe-based OC. However, both Cu and CuO have a low melting point and a high tendency for agglomeration [30]. Perovskite-type materials have also been investigated for chemical looping processes [31], but their relatively low reactivity and oxygen transport capacity limit their practical application.

Fe-based materials are considered promising OCs due to their abundance, low cost and non-toxicity. Consequently, they have been widely studied for use in chemical looping processes [32–35]. Iron exists in three oxidation states, Fe_2O_3, Fe_3O_4, and FeO. The reduction of the latter two, i.e., Fe_3O_4 and FeO, require high CO/CO_2 or H_2/H_2O ratio to proceed, which thermodynamically favors syngas production [36,37]. The low reactivity of Fe-based OC towards methane, however, results in insufficient fuel conversion in chemical looping processes. Pans et al. [38] investigated chemical looping combustion (CLC) of different gases and found the fuel conversion was high for syngas (H_2 and CO), but low for methane-containing gases. Other studies confirmed the reactivity of Fe-oxides with gases encountered in methane reforming ranking as $H_2 > CO > CH_4$ [39]. The reduction rates of the various Fe-oxides also differ one from another. At temperatures above 576 °C, the reduction of Fe_2O_3 consists of three stages, Fe_2O_3->Fe_3O_4, Fe_3O_4->FeO, and FeO->Fe. While the first stage is the fastest, the latter two are intrinsically successively slower [40–42]. To improve the fuel conversion in chemical looping processes using Fe-based OC, Ni-based materials have been studied as additives [43–45], whereas safety and environmental concerns arise. In contrast, noble-metal catalysts, such as Pt-, Rh-, Ru-, and Ir-based catalysts are known to be active for methane reforming [46–50], but their use in aCLR has not been widely studied. Another reason to consider a noble-metal catalyst is that, the feed steam-to-carbon (S/C) ratio is typically low in the aCLR FR, which favors coke formation, and further induces catalyst deactivation [51,52]. Noble-metal catalysts usually have a lower coke formation tendency [53] than Ni-based catalysts, which makes them particularly attractive for aCLR. Finally, Rh is non-toxic, whereas Ni is known to be cancerogenic [54,55]. By combining an Fe-based OC and a noble metal catalyst, a new process called catalyst-enhanced aCLR (CE-aCLR) is proposed, which enhances the methane conversion whilst retaining environmental compatibility.

To study the commercial scale feasibility of the CE-aCLR, an advanced simulation model is required that accounts for the unique features of the materials and reactors. For instance, in the FR of the CE-aCLR, the catalyst takes only a few percentages of the solids, and the fast SMR reactions are typically limited by mass transfer limitations [12]. Thus, the pseudo-homogeneous emulsion phase assumption in the classical two-phase fluidized bed model must be improved to correctly simulate the methane conversion process, which is done by accounting for the mass transfer between the emulsion gas and catalyst particles external surface. In addition, because the various Fe-oxides exhibit different reduction rates, the influence of the residence time distribution (RTD) of the OC particles has to be accounted for to correctly simulate the reduction of the OC. Thus, an effectiveness factor was introduced and will be discussed in detail later. The developed model applies various scale-bridging approaches to account appropriately for the various physical/chemical phenomena while ensuring acceptable simulation times. The model allows evaluating the influence of material properties such as reaction kinetics, reactor design and operating conditions.

Knowing the intrinsic kinetics of noble metal-based catalyst is the prerequisite for evaluating the feasibility of CE-aCLR. As previous kinetic studies on SMR mostly focused on Ni-based catalysts, the intrinsic kinetics of a commercial Rh-based catalyst is first determined with carefully designed experiments that eliminated the heat and mass transfer limitations and ensure isothermal operation. Next, a multi-scale reactor model is presented that is used to evaluate commercial CE-aCLR performance. The primary contributions of work are:

- Proposed environmentally friendly CE-aCLR,
- Investigation of the intrinsic kinetics of a very active commercial Rh-based SMR catalyst.
- Extension of a previously developed and verified multi-scale model [56] to simulate CE-aCLR, accounting for the effect of RTD of the solids in the FR on the reduction reactions, and for mass transfer limitations between the emulsion gas and catalyst particles.
- Demonstration of the feasibility of the novel CE-aCLR process by the means of numerical simulations. Sensitivity studies of the influence of the bed height, the catalyst activity, and the reactivity of OC on the process performance.

2. Experimental

This section presents the study of the intrinsic kinetics of a Rh-Based SMR catalyst.

2.1. Catalyst and characterization

A commercial Rh-based catalyst with 5% Rh on α-Al_2O_3 as active phase was selected as the catalyst for the CE-aCLR. The catalyst was crushed and sieved to the desired diameter range, i.e., 100–150 μm. The

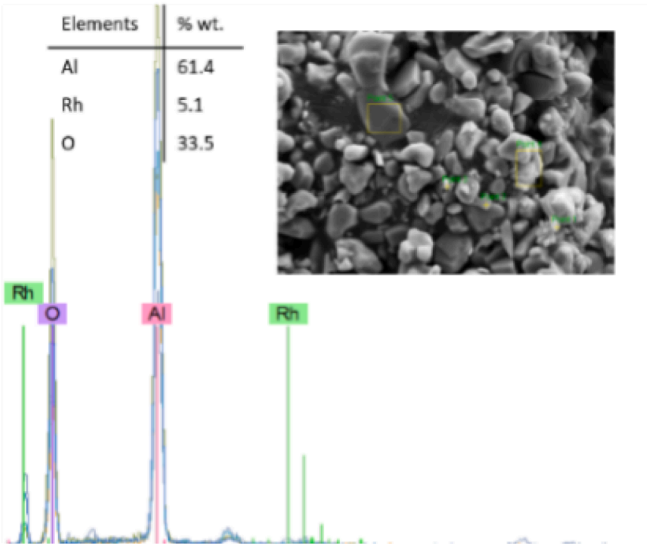

Fig. 1. SEM image and EDX elemental analysis of the Rh-based SMR catalyst.

morphology and EDX-elemental analysis of the catalyst are shown in Fig. 1.

2.2. Experimental reactor design and operation conditions

The experimental reactor was designed to allow determining the intrinsic reaction kinetics of the very fast and endothermic SMR reactions. In order to facilitate the kinetic modeling, the bed design and experimental conditions were carefully chosen to allow operating the reactor isothermally and under plug flow, in the absence of interfacial and intra-particle mass and heat transfer limitations, and with a small pressure drop across the bed [57]. Criteria to satisfy these conditions were summarized by Minette et al. [58], and lead to a relatively narrow window of operating conditions.

A schematic of the experimental setup is shown in Fig. 2 (left). The gases were provided by Air Liquide: Argon Alpha 1, CH_4 N35, H_2 N40, and CO_2 N27. The individual flow rates of the gases were controlled using calibrated thermal mass flow controller (MFC) (SLA5850, Brooks Instrument). Deionized water was fed from a pressurized tank, using Argon at about 2 bar higher than the operating pressure of the reactor. The water flow rate was controlled using a calibrated Coriolis mass flow controller (QMBC2, Brooks Instrument). The reactor was made from an Inconel-625 tube with an inner diameter of 10 mm. A 6 mm thermowell was inserted into the reactor center for measuring the bed temperature, resulting in an annular reactor bed that also decreased the effective diameter and the radial temperature difference of the bed. The reactor is installed in an 800 W electrically heated furnace (Kamenev Liege) controlled by a programmable PID controller with a thermocouple installed in the thermowell. Besides, the pressure at the reactor inlet and outlet were measured using two pressure transmitters (PN300, NEXON) to verify the pressure drop. The catalyst (15.6 mg) was mixed with alumina particles (100–150 μm in diameter) to compose about 1 g mixture to be a 20 mm long bed that was loaded in the mid of the heated zone. The rest of the bed was filled with coarse alumina particles to minimize the pressure drop in the inert bed. Details about the bed packing are given in Fig. 2 (right).

To determine the intrinsic reaction kinetics, various criteria must be satisfied that lead to a narrow window of operation conditions, in particular for the temperature. These criteria have been discussed by [58]. To widen the temperature range and increase the accuracy of the kinetic parameter estimation, both SMR and the reverse reaction, methanation and reverse WGS, were experimentally studied. The

Table 1
Test conditions for the steam methane reforming and methanation and RWGS experiments.

Steam methane reforming	
Temperature (°C)	450 – 525
Pressure (bar)	5
S/C molar	3
H_2/CH_4 molar	1 – 1.5
Ar/Cmolar	6–10 (Ar/C)
Flow rate of CH_4	300–400 Nml/min
Methanation and reverse of water gas shift	
Temperature (°C)	375–450
Pressure (bar)	5
H_2/CO_2 molar	2–4
Ar/H_2 molar	6
Flow rate of CO_2	100–250 Nml/min

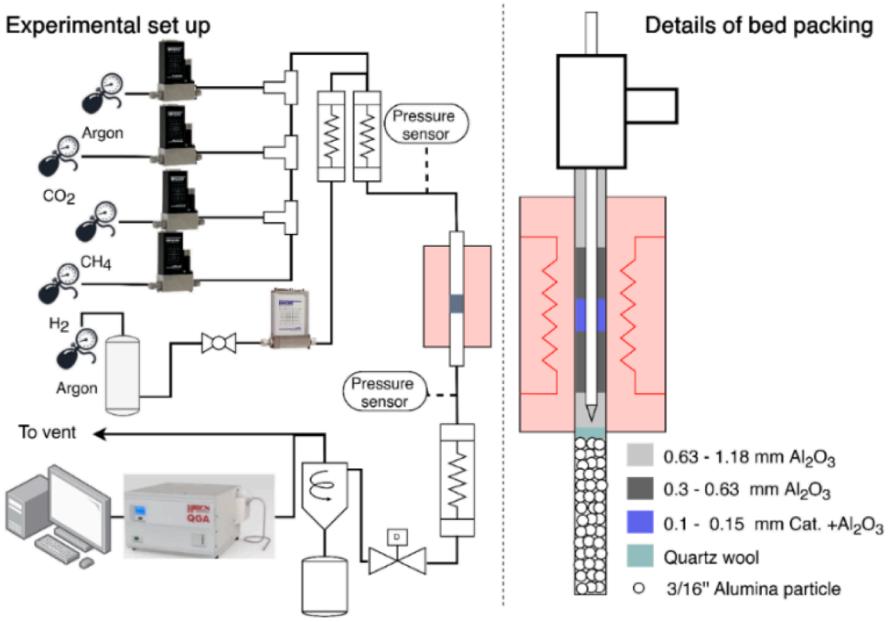

Fig. 2. (Left) schematic diagram of the experimental set-up, (Right) detailed schematics of the micro-fixed bed reactor.

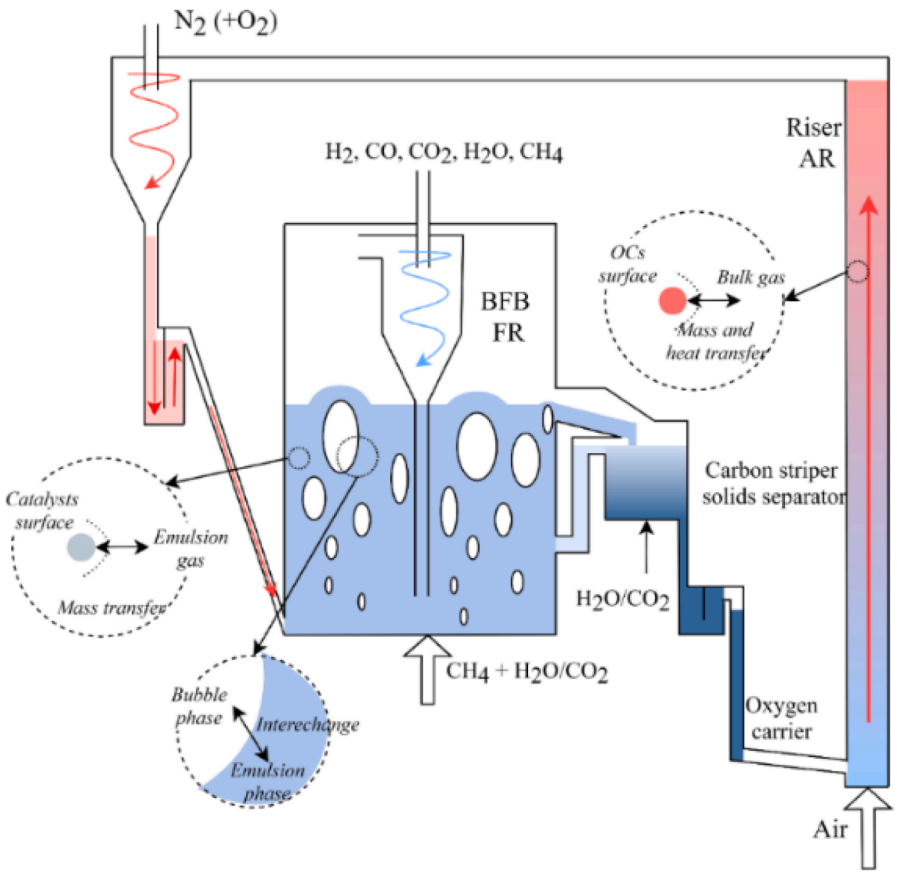

Fig. 3. Schematic representation of the simulated CE-aCLR system and the involved physical phenomena.

experimentally tested conditions are summarized in Table 1. Five different space-times W/F^0_{CH4} were tested for each operating temperature. The tested temperatures for SMR were lower than that in typical industrial practice to guarantee negligible temperature gradients and to avoid approaching chemical equilibrium. Hydrogen was co-fed aiming at slowing down the methane reforming reactions to guarantee isothermal operation [28,59].

The feed water was vaporized in an evaporator operating at 230 °C, then mixed with other gases. The gas mixture passed through a superheater before entering the reactor. The operating temperature of the preheater was 450 °C or 250 °C respectively for SMR and methanation. Immediately after exiting the reactor, the reactor effluent was cooled in a coil immersed in a chamber with a circulating water-*iso*-propanol mixture kept at 5 °C by a chiller. After passing through a pressure regulator (LF-Series, Equilibar), the condensed water and gas were separated by a sample filter (91S6, Parker) to remove the liquid and possible dust. The dry effluent was then analyzed using a mass spectrometer (QGA, Hiden Analytical) for quantitative analysis of H_2, CH_4, CO, CO_2, and Ar at m/z of 2, 15, 28, 44, and 40 respectively. The mass spectrometer was calibrated before every test with a gas mixture close to the dry gas composition to ensure accuracy. It was verified that the deviation of the carbon balance and the reaction stoichiometry were less than 5% for every test.

Prior to kinetic testing, the catalyst was reduced for 12 h with a 10/90% H_2/Ar mixture at 575 °C at 5 bar. The temperature was then decreased to 525 °C for catalyst aging at reference conditions. Typically, the activity of the catalyst decreased rapidly in the first few hours and then decreased more slowly. The catalyst aging was thus performed for about 24 h until the catalyst activity was considered sufficiently stable. Before testing at each temperature–pressure combination, a reference test ($F_{CH4} = 300$Nml/min, S/C = 3, Ar/CH_4 = 6, H_2/CH_4 = 1.2 at 500 °C) was performed to verify stable catalyst activity and to allow minor correction of the space–time, following the procedure described by Xu and Froment [28], to account for an eventual change of activity.

2.3. Reaction mechanism and parameter estimation

The following three global reactions (r1), (r2) and (r3) are considered to take place on the catalyst [28]:

$$CH_4 + H_2O \leftrightarrow CO + 3H_2, \Delta H^0_r = 206 kJ/mol \quad (r1)$$

$$CO + H_2O \leftrightarrow CO_2 + H_2, \Delta H^0_r = -41 kJ/mol \quad (r2)$$

$$CH_4 + 2H_2O \leftrightarrow CO_2 + 4H_2, \Delta H^0_r = 165 kJ/mol \quad (r3)$$

The reactions (r1) - (r3) are assumed to take place on the same active sites. The reaction mechanism, introduced by Xu and Froment [28], is adopted and described in Supplementary Material. The signature of this reaction mechanism is the formation of adsorbed CH_xO-*l* species that were confirmed by Menon et al. [60]. The elementary steps involved in each global reaction are described in Supplementary Material. It is well accepted that steps (s7), (s8), and (s9) are the rate-determining steps for respectively the global reaction (r1), (r2), and (r3) [58,61], and the corresponding Langmuir-Hinshelwood-Hougen-Watson-type rate expression are listed in Eqs. (1)–(3):

$$r_1 = \left(\frac{k_1}{p^{2.5}_{H_2}}\right)\left(p_{CH_4}p_{H_2O} - \frac{p_{CO}p^3_{H_2}}{K_I}\right)\frac{1}{DEN^2} \quad (1)$$

$$r_2 = \left(\frac{k_2}{p_{H_2}}\right)\left(p_{CO}p_{H_2O} - \frac{p_{H_2}p_{CO_2}}{K_{II}}\right)\frac{1}{DEN^2} \quad (2)$$

$$r_3 = \left(\frac{k_3}{p_{H_2}^{3.5}}\right)\left(p_{CH_4}p_{H_2O}^2 - \frac{p_{CO_2}p_{H_2}^4}{K_{III}}\right)\frac{1}{DEN^2} \quad (3)$$

$$DEN = 1 + K_{CH_4}p_{CH_4} + K_{CO}p_{CO} + K_{H_2}p_{H_2} + K_{H_2O}p_{H_2O}/p_{H_2} \quad (4)$$

In SMR experiments, methane conversion and the selectivity to CO_2 are respectively defined as:

$$x_{CH_4} = \left(F_{CH_4}^0 - F_{CH_4}\right)\Big/F_{CH_4} \quad (5)$$

$$s_{CO_2} = F_{CO_2}/F_{CH_4}^0 \quad (6)$$

In methanation and RWGS experiments, the conversion of CO_2 and conversion to CH_4 are defined as:

$$x_{CO_2} = \left(F_{CO_2}^0 - F_{CO_2}\right)\Big/F_{CO_2}^0 \quad (7)$$

$$s_{CH_4} = F_{CH_4}/F_{CO_2}^0 \quad (8)$$

The integral method of kinetics analysis was used to estimate the rate parameters [57,62,63]. The conversions were calculated by integrating the continuity equations for reference components. The model equations are listed in Supplementary Material. The Athena Visual Studio software was used for parameter estimation and statistical testing.

3. Modeling

This section presents the model for the CE-aCLR reactor system.

3.1. Overview

The dual fluidized bed reactor system is considered for the CE-aCLR process as this configuration has been successfully demonstrated to be suitable for various chemical looping processes [17,22,64,65]. The aCLR system mainly consists of a riser AR where the OC is oxidized by air, a bubbling fluidized bed (BFB) FR where methane is converted, and a carbon stripper in which the carbon-containing species are removed from the solids before the solids are transported to the AR for oxidation. The carbon stripper can also act as a segregator that separates the OC and the catalysts. The CE-aCLR bed reactor system is schematically illustrated in Fig. 3.

The CE-aCLR model considers that the Fe-based OC is only responsible for transferring oxygen between the AR and the FR, while the Rh-based SMR catalyst is considered to catalyze the methane reforming reactions in the FR. The OC and catalyst are mixed in the FR and are separated outside the FR. The two kinds of solids are considered to have different densities. Typically, the Fe-based OC has a higher density while the SMR catalyst is lighter as it is typically a few percentages of active metal on porous ceramic in order to have high activity. In general, the segregation of two kinds of particles can be severe when the superficial gas velocity is close to u_{mf} but is attenuated as bubbling becomes more vigorous [66,67]. Joseph et al. [68] found at a superficial gas velocity greater than 3 times the minimum fluidization velocity (u_{mf}), the binary mixture of two particles that differ in both density and size were well-mixed. Thus, the catalyst and OC are seen as well-mixed in the FR in this work as the superficial gas velocity is usually 5–10 times the u_{mf} in aCLR [22]. On the other hand, Chladek et al. [69] found that segregation can be obtained with suitable gas velocity within the interval of the two u_{mf}. When the two particles have close u_{mf}, e.g., 0.36 m/s and 0.26 m/s in [70], segregation was obtained when the gas velocity was between the u_{mf} of the lighter and heavier particles. The bottom bed consisted of $>$ 99% jetsam, i.e., the particles tend to sink, while the top layer was much less pure with 24% jetsam. Other approaches have also been tested to improve the segregation efficiency, including vibration [71], and pulsating gas flow [72]. Achieving a pure heavier OC particles flow to send from the FR to the AR is as such feasible as assumed in this work.

After separation, the OC is transported to the AR for oxidation, while the catalyst is recycled into the FR. Also, because the noble-metal-based catalysts are usually very active in catalyzing SMR reactions, the OC typically takes a much larger volume fraction in the FR than the catalyst.

3.2. Reactivity of the OC

An Fe-based, $MgAl_2O_4$-supported OC with 20% Fe_2O_3 when fully oxidized is considered in this work. $MgAl_2O_4$ is selected as carrier as it has a very high melting point and interacts weakly with the active metals [73,74]. Hu et al. [24] found that the oxygen transport capacity of 20% Fe_2O_3 on $MgAl_2O_4$ was stable during reduction and oxidation (RedOx) cycles. It had also little tendency towards agglomeration and sintering, while other oxygen carriers containing 30%, 40%, and 50% Fe_2O_3 defluidized during RedOx cycles. The defluidization and sintering of the OC are the result of high temperatures during oxidation. In aCLR where no heat should be deliberately extracted, the OC with 20% Fe_2O_3 in the OC is more than enough for the oxidized OC to reach the temperature limit (for OC activity and metallurgical considerations). It is assumed that the diameter of the OC particles is in the range of 180–220 μm while its density is 2500 kg/m^3. The reactivity will be discussed in the following subsections. Note that the concentration of species, i.e., $C_{Fe_2O_3}$, $C_{Fe_3O_4}$, C_{FeO}, and $C_{Fe_3O_4}$ are always expressed with respect to fully oxidized OC in this work.

3.2.1. Reduction kinetics of the OC

The reduction of different Fe-based OCs has been extensively studied. The consensus is that the reduction of Fe_2O_3 follows Fe_2O_3->Fe_3O_4->Fe at a temperature lower than 576 °C, while at higher temperature, it follows Fe_2O_3->Fe_3O_4->FeO->Fe [36,40,75]. Abad et al. [39,76] investigated the reduction of different types of iron ore with H_2 and CO with varying H_2O and CO_2 concentrations and concluded that the reduction of Fe_2O_3 to Fe_3O_4 is barely affected by the presence of H_2O and CO_2 while the further reduction reactions are significantly affected. Thus, in this work, the reduction of Fe_2O_3 to Fe_3O_4 is considered irreversible, while Fe_3O_4 to FeO and FeO to Fe are considered reversible. The reduction reactions with H_2 and CO are as follow:

$$3Fe_2O_3 + H_2(CO) \rightarrow 2Fe_3O_4 + H_2O(CO_2), \Delta H_r^0 = -5.8(-47.0)\text{kJ/mol}$$

$$Fe_3O_4 + H_2(CO) \leftrightarrow 3FeO + H_2O(CO_2), \Delta H_r^0 = 60.6(19.3)\text{kJ/mol}$$

$$FeO + H_2(CO) \leftrightarrow Fe + H_2O(CO_2), \Delta H_r^0 = 30.2(10.9)\text{kJ/mol}$$

The reduction rates of Fe_2O_3, Fe_3O_4 and FeO reacting with H_2, CO and CH_4 have to be considered [77], but have been reported separately in the literature. The first stage reduction is very fast, whereas the second and third stages are much slower [42,78]. In addition, it is found that hematite is fastest reduced by H_2, followed by CO, and slowest by CH_4 [39,42,78,79]. It has been shown by Liu et al. [42] that there is no competing nor synergistic effect in the reduction of Fe-base OC by H_2 and CO. Thus, the reduction reactions are assumed independent in this work.

The reduction kinetics from four papers [39–42] are adopted to represent the fast reduction kinetics of the synthesized Fe-based OC. Buelens et al. [40] used in-situ XRD to study the reduction of an OC, Fe_2O_3 on $MgAl_2O_4$, by H_2 and confirmed the reduction of Fe_2O_3 being a three-stage reaction. The reduction kinetics was determined by the means of non-isothermal reduction experiments. The shrinking core model was used to describe the sequenced reduction processes. The rate expression is as follow:

$$r_{i,H_2}\left[\frac{mol_i}{kg_{OC}\cdot s}\right] = \frac{3}{r_0\rho_{Fe_2O_3}^M}\frac{a\cdot C_{Fe_2O_3}\left(C_{H_2} - C_{H_2O}/K_{eq,i}\right)}{\frac{1}{k_{i,H_2}}(1-X_i)^{-2/3} + \frac{r_0}{D_i}\left[(1-X_i)^{-1/3} - 1\right]} \quad (9)$$

where i = Fe_2O_3, Fe_3O_4, FeO, r_0 is the average grain radius = 5.3•10^{-8}

Table 2
Equilibrium constants for reactions R5-R6 and R5′-R6′ [36].

Reaction-Temperature range/°C	$K_{eq,ri} = \exp(a + b/T)$	
	a	b
R5-(576 ~ 1377 °C)	7.563	−7393.9
R6-(576 ~ 1377 °C)	1.239	−2023.8
R5′-(576 ~ 1377 °C)	3.661	−3132.5
R6′-(576 ~ 1377 °C)	−2.667	2240.6

[m], ρ^{M}_{Fe2O3} is the molar density of $Fe_2O_3 = 7.82\bullet10^3$ [mol/m^3], a = 3, 1, 1 respectively for Fe_2O_3, Fe_3O_4 and FeO, $k_{i,H2} = A_{0,i,H2}\exp(-E_{a,i,H2}/RT)$, $D_i = D_{0,i}\exp(-E_{a,diff,i,H2}/RT)$. For the reduction of Fe_2O_3 by CO, the kinetics reported by Bohn et al. [41] is adopted for the first and second step reduction, while Liu et al.'s work [42] is adopted for the third step. For the first stage ($Fe_2O_3 \rightarrow Fe_3O_4$):

$$r_{Fe_2O_3,CO}\left[\frac{mol_{Fe_2O_3}}{kg_{OC}\cdot s}\right] = k_{Fe_2O_3,CO}\left(C_{CO} - \frac{C_{CO_2}}{K_{eq,R5'}}\right)\left(1 - X_{Fe_2O_3}\right)^{0.4} \quad (10)$$

For the second stage ($Fe_3O_4 \leftrightarrow FeO$):

$$r_{Fe_3O_4,CO}\left[\frac{mol_{Fe_3O_4}}{kg_{OC}\cdot s}\right] = k_{Fe_3O_4,CO}\left(C_{CO} - \frac{C_{CO_2}}{K_{eq,R6'}}\right)\left(1 - X_{Fe_3O_4}\right)^{1.2} \quad (11)$$

For the third stage ($FeO \leftrightarrow Fe$):

$$r_{FeO,CO}\left[\frac{mol_{FeO}}{kg_{OC}\cdot s}\right] = \frac{S_0\cdot C_{FeO}}{1-\varepsilon_0}\frac{k_{FeO,CO}\sqrt{1-\psi\ln(1-X_{FeO})}}{1+\frac{\beta\alpha}{\psi}\left[\sqrt{1-\psi\ln(1-X_{FeO})}-1\right]}\left(C_{CO} - \frac{C_{CO_2}}{K_{eq,R7'}}\right) \quad (12)$$

where $k_{i,CO} = k_{0,i,CO}\bullet\exp(E_{ai,CO}/RT)$, i = Fe_2O_3, Fe_3O_4 and FeO, α is the ratio of the molar volume of solid product to reactant, $\beta = 2k_{FeO,CO}(1-\varepsilon_0)/V_{FeO}S_0D_{FeO,CO}$, $\psi = 4\pi L_0(1-\varepsilon_0)/S_0^2$, $S_0 = (2.5 \pm 1.2) \times 10^6$ [m^{-1}], $L_0 = 7.5 \times 10^{12}$ [m^{-2}], $\varepsilon_0 = 0.6$, $V_{FeO} = 1.25 \times 10^{-5}$ [m^3/mol], $D_{FeO,CO} = 2.91 \times 10^{-7}\cdot\exp(-90 \times 10^3/RT)$ [m^2/s]. The equilibrium constants for the reduction of magnetite and wustite are given in Table 2. In the simulation, CO and H_2 are considered to react with magnetite only when the driving forces, $(C_{H_2} - C_{H_2O}/K_{R5})$ and $(C_{CO} - C_{CO_2}/K_{R5'})$ are both positive, and only react with wustite when both $(C_{H_2} - C_{H_2O}/K_{R6})$ and $(C_{CO} - C_{CO_2}/K_{R6'})$ are positive (which is valid at any location in the FR during autothermal operation).

The reactivity of hematite with CH_4 is typically low as has been shown from TGA tests [80] and fluidized bed experiments [38,81,82]. It is widely accepted that CH_4 is fully oxidized into H_2O and CO_2 when Fe_2O_3 is reduced to Fe_3O_4. Although reduction of Fe_2O_3 to Fe by CH_4 with high methane conversion has been shown in the literature [37,83], very high spacetimes, W/F_0, were used in these studies, which is also evidence of the very slow reduction of magnetite and wustite with CH_4. Therefore, the reduction of magnetite and wustite by CH_4 are neglected in this work. This treatment hardly brings any error because the OC only reacts with the gas in the emulsion phase in a fluidized bed, and it is shown that the concentration of CH_4 in the emulsion phase is relatively low compared to that of H_2 and CO [56]. The reaction kinetics reported by Mendiara et al. [39] is adopted for the reduction of Fe_2O_3 to Fe_3O_4 by CH_4:

$$CH_4 + 12Fe_2O_3 \rightarrow CO_2 + 2H_2O + 8Fe_3O_4, \Delta H_r = 141.6\text{kJ/mol} \quad (r7)$$

$$r_{Fe_2O_3,CH_4}\left[mol_{Fe_2O_3}/kg_{OC}\cdot s\right] = k_{Fe_2O_3,CH_4}\cdot C_{CH_4}(1-X)^{\frac{2}{3}} \quad (13)$$

According to Buelens et al. [40], the conversion of each step is calculated with:

$$x_{Fe_2O_3} = 1 - C_{Fe_2O_3}/C^{fullOx}_{Fe_2O_3} \quad (14)$$

$$x_{Fe_3O_4} = x_{Fe_2O_3} - 3C_{Fe_3O_4}/2C^{fullOx}_{Fe_2O_3} \quad (15)$$

Table 3
Kinetic parameters for the three-stage reduction of Fe_2O_3 by H_2, CO and CH_4 [39–42].

Gaseous reactant	Solid reactant	Parameter	unit	Value
H_2 [40]	Fe_2O_3	$A_{0,Fe2O3,H2}$	[m/s]	$1.2 \pm 0.2 \times 10^8$
		$E_{a,Fe2O3,H2}$	[kJ/mol]	191.1 ± 0.8
		$D_{0Fe2O3,H2}$	[m^2/s]	$2.8 \pm 0.3 \times 10^{-12}$
		$E_{a,diff,Fe2O3,H2}$	[kJ/mol]	37.5 ± 0.6
	Fe_3O_4	$A_{0,Fe3O4,H2}$	[m/s]	$2.2 \pm 0.1 \times 10^2$
		$E_{a,Fe3O4,H2}$	[kJ/mol]	129.2 ± 0.3
		$D_{0,Fe3O4,H2}$	[m^2/s]	$1.8 \pm 0.2 \times 10^{-9}$
		$E_{a,diff,Fe4O4,H2}$	[kJ/mol]	86.9 ± 0.4
	FeO	$A_{0,FeO,H2}$	[m/s]	$1.5 \pm 0.1 \times 10^2$
		$E_{a,FeO,H2}$	[kJ/mol]	120.2 ± 0.2
		$D_{0,FeO,H2}$	[m^2/s]	$3.8 \pm 0.2 \times 10^{-9}$
		$E_{a,diff,FeO,H2}$	[kJ/mol]	99.0 ± 0.3
CO [41,42]	Fe_2O_3	$A_{0,Fe2O3,CO}$	[m^3/kg$_{OC}\bullet$s]	3.88×10^3
		$E_{a,Fe2O3,CO}$	[kJ/mol]	75
	Fe_3O_4	$A_{0,Fe3O4,CO}$	[m^3/kg$_{OC}\bullet$s]	1.85×10^4
		$E_{a,Fe3O4,CO}$	[kJ/mol]	94
	FeO	$A_{0,FeO,CO}$	[m^4/mol$\bullet$s]	1.1×10^{-6}
		$E_{a,FeO,CO}$	[kJ/mol]	64
		$D_{0,FeO,CO}$	[m^2/s]	2.91×10^{-7}
		$E_{a,diff,FeO,CO}$	[kJ/mol]	90
CH_4 [39]	Fe_2O_3	$A_{0,Fe2O3,CH4}$	[m^3_g/kg$_{OC}\bullet$s]	1.46×10^{10}
		$E_{a,Fe2O3,CH4}$	[kJ/mol]	257

$$x_{FeO} = x_{Fe_3O_4} - C_{FeO}/2C^{fullOx}_{Fe_2O_3} \quad (16)$$

The kinetic parameters used to calculate the reaction rates are given in Table 3. The conversion-time curves with the adopted kinetics are shown in Figure S2, with the gas concentrations chosen similar to those in the emulsion phase in aCLR operation.

3.2.2. Oxidation of the OC

The oxidation of the Fe-based materials is very fast. Grosvenor et al. found that, at room temperature, Fe is oxidized by O_2 to form a layer of Fe_2O_3, and cationic diffusion happens afterward to form Fe_3O_4 [84,85]. When Fe is oxidized by CO_2 or H_2O, in-situ XRD demonstrated that the Fe is oxidized directly to Fe_3O_4 without FeO being the intermediate product [40]. When Fe is oxidized with O_2, the ex-situ XRD study revealed the existence of FeO and Fe_3O_4 in the partially oxidized OC and the product of full oxidation is Fe_2O_3 [86,87]. Because of its very fast nature, it is assumed that the oxidation of Fe with O_2 is a single-step process to Fe_2O_3. The solid-state transformation occurs when the OC is in O_2-depleted conditions, forming different oxides according to the reaction stoichiometry. The oxidation reaction and the transformation from Fe_2O_3 to other Fe-oxides is described by:

$$Fe + 0.75O_2 \rightarrow 0.5Fe_2O_3, \Delta H^0_r = -412.1\text{kJ/mol} \quad (r8)$$

$$4Fe_2O_3 + Fe \rightarrow 3Fe_3O_4, \Delta H^0_r = -58.2\text{kJ/mol} \quad (r9)$$

$$Fe_3O_4 + Fe \rightarrow 4FeO, \Delta H^0_r = 30.2\text{kJ/mol} \quad 10)$$

The equivalent Fe_2O_3 concentration is used during the oxidation in the AR, which requires the equivalent Fe_2O_3 concentration of the OC at the exit of the FR as the feed condition for the AR:

$$C^{eqvoutFR}_{Fe_2O_3} = C^{outFR}_{Fe_2O_3} + \left(4C^{outFR}_{Fe_3O_4} + C^{outFR}_{FeO}\right)/3 \quad (17)$$

The composition of OC after solid-phase transformation is calculated according to the equivalent Fe_2O_3 concentration at the exit of the AR. If $C^{outAR}_{Fe_2O_3} \geq \frac{8}{9}C^{fullox.}_{Fe_2O_3}$, Fe is present as Fe_2O_3 and Fe_3O_4:

$$\begin{cases} C_{Fe_3O_4}^{inFR} = 6\left(C_{Fe_2O_3}^{fullox} + C_{Fe_2O_3}^{outAR}\right) \\ C_{Fe_2O_3}^{inFR} = 9C_{Fe_2O_3}^{outAR} - 8C_{Fe_2O_3}^{fullox} \end{cases} \quad (18)$$

If $2C_{Fe_2O_3}^{fullox} \le 3C_{Fe_2O_3}^{outAR} < \frac{8}{3}C_{Fe_2O_3}^{fullox}$, Fe is present as Fe_3O_4 and FeO:

$$\begin{cases} C_{Fe_3O_4}^{inFR} = 3C_{Fe_2O_3}^{outAR} - 2C_{Fe_2O_3}^{fullox} \\ C_{FeO}^{inFR} = 8C_{Fe_2O_3}^{fullox} - 9C_{Fe_2O_3}^{outAR} \end{cases} \quad (19)$$

If $3C_{Fe_2O_3}^{outAR} \le 2C_{Fe_2O_3}^{fullox}$, Fe is present as FeO and Fe:

$$\begin{cases} C_{FeO}^{inFR} = 3C_{Fe_2O_3}^{outAR} \\ C_{Fe}^{inFR} = 2C_{Fe_2O_3}^{fullox} - 3C_{Fe_2O_3}^{outAR} \end{cases} \quad (20)$$

The evolution of the temperature between the AR and FR is calculated from the enthalpy balance for the OC:

$$\sum_i h_i m_i = \sum_k h_k m_k \quad (21)$$

Where i denotes the Fe-oxides at the exit of the AR/FR and k denotes the Fe-oxides at the inlet of the FR/AR. The oxidation of Fe by O_2 is extremely fast at high temperatures, explaining why many studies were almost not able to distinguish the difference in oxidation rate at different temperatures [39,78,88]. Our previous work [89] found that the oxidation of an Fe-based OC (20% wt. Fe_2O_3 on $MgAl_2O_4$) was even significantly faster than the rates typically reported in the literature. An empirical rate equation proposed in [89] is adopted in this work:

$$r_{O_2} = 0.75 r_{Fe} = k_0 \exp\left(-\frac{E_a}{RT}\right)(1 - x_{Fe}) p_{O_2} \quad (22)$$

Note that a homogeneous solid-phase transformation was assumed for the Fe-based OC and that a first-order dependent with respect to the partial pressure of O_2 was observed. The low activation energy of Fe oxidation with O_2, 32 kJ/mol, reported by Grosvenor et al. [84], was used for extrapolation. This activation energy results in a pre-exponential factor, k_0, of 3.436E + 03 *[mol_{O2}/kg_{OC}·bar·s]*. It should be noted that the used pre-exponential factor is still somewhat an underestimation as transport limitations could not be entirely eliminated during the oxidation experiments.

3.3. Reactor hydrodynamic models

The aCLR model was based on the standard two-phase model [90] for BFBs and the 1-D heterogeneous model for riser type reactor. The base model was developed elsewhere and verified against experimental data in pilot scale experiments [56]. The model is extended in this work to account for the use of a separate Fe-based OC and Rh-based SMR catalyst in the CE-aCLR, the low catalyst volume fraction, and multiple oxidation states of the Fe-based OC. These modifications to the simulation model are discussed in detail thereafter.

The two-phase model for the FR assumes that the BFB consists of a solids-free bubble phase and an emulsion phase containing all the particles that are at minimum fluidization conditions. Bubbles are initially small and grow larger when traveling upwards until reaching the top of the bed or breaking up [91]. A maximum bubble diameter is typically reached. Slugging is not observed when the reactor is sufficiently large [92]. Plug flow is considered for the bubble phase because of the high bubble rise velocity, while axial dispersion of the emulsion phase gas must be considered to account for the gas dispersion induced by the solids back-mixing. Two mechanisms contributing to mass transfer between bubble and emulsion phase are accounted for: 1) molecular diffusion driven by species concentration differences, 2) excess flow due to volume expansion induced by the reaction involving CH_4. The former is modeled by the interchange coefficient, k_I, while the latter is accounted for by an excess flow term, $\Delta F_{A,Ei}$. Typically, the reduction

Table 4
Reactor model equations for the BFB FR and riser AR.

FR
$\frac{dF_A^b}{dz} = -k_I\left(C_A^b - C_A^b\right) + \Delta F_{A,Ei}$
$\frac{dF_A^e}{dz} = \frac{d}{dz}\left(\frac{D_{eg}}{f_{eg}u_{eg}}\frac{dF_A^e}{dz}\right) + k_I\left(C_A^b - C_A^e\right) - k_g a_v\left(C_A^e - C_A^s\right) + f_{es}\alpha_{OC}\rho_{OC}\varphi_{Red}R_A^{Red} + R_A^{WGS} - \Delta F_{A,Ei}$
$k_g a_v\left(C_A^e - C_A^s\right) = f_{es}\alpha_{cat}\rho_{cat}R_A^{SMR}$
$\frac{\dot{m}_s}{\Omega_r}\frac{dC_i}{dz} = \rho_{OC}f_{es}\alpha_{OC}D_{es}\frac{d^2C_i}{dz^2} + \varphi_{red}\rho_{OC}f_{es}\alpha_{OC}R_i$
$m_s^{inFR}h_s\left(T_s^{inFR}\right) + \sum_A m_A^{inFR}h_A\left(T_g^{inFR}\right) = m_s^{outFR}h_s(T_{FR}) + \sum_A m_A^{inFR}h_A(T_{FR})$
$\frac{dp}{dz} = -f_{es}(\alpha_{OC}\rho_{OC} + \alpha_{cat}\rho_{cat})g$
AR
$\frac{dF_{O_2}}{dz} = -k_g a_v\left(C_{O_2} - C_{O_2}^s\right)$
$\frac{\dot{m}_s}{\Omega_r\rho_s}\epsilon_s\frac{dC_{O_2}^s}{dz} = k_g a_v\left(C_{O_2} - C_{O_2}^s\right) + r_{O_2}\rho_{OC}(1-\varepsilon_g)$
$\frac{\dot{m}_s}{\Omega}\frac{dC_{Fe}}{dz} = -r_{Fe}\rho_{OC}(1-\varepsilon_g)$
$u_{sg}\rho_g\overline{C_{p,g}}\frac{dT}{dz} = -h_f a_v(T - T_s)$
$\frac{\dot{m}_s C_{p,s}}{\Omega}\frac{dT_s}{dz} = h_f a_v(T - T_s) + r_{Fe}\left(-\Delta H_{Ox}^r\right)\rho_s(1-\varepsilon_g)$
$-\frac{dp_{tot}}{dz} = \rho_{OC}g(1-\varepsilon_g) + \rho_g g\varepsilon_g + \frac{2\eta_s\rho_{OC}u_{ss}^2}{(1-\varepsilon_g)D_{AR}} + \frac{2\eta_g\rho_g u_{sg}^2}{\varepsilon_g D_{AR}}$

reaction rates are calculated using the concentration of species in the emulsion gas, assuming the mass transfer between emulsion gas and the OC is fast. This is justified by the relatively low reaction rates and high concentrations of gaseous reactants in the emulsion phase, i.e., H_2 and CO [56,57]. For the fast SMR reactions on the catalyst, however, interfacial mass transfer between emulsion gas and catalyst has to be explicitly accounted for.

For the solids phase species in the FR, because the reduction rates of Fe in different oxidation states are very different, the reduction of each oxide has to be modeled separately. Solids mixing also significantly affects the reduction rate. A model based on plug flow with axial dispersion is adopted to account for the back-mixing of the solids. The high effective diffusivity of the solids phase results, however, in a very uniform solids concentration within the FR. This is the volume-averaged concentration, however, with individual OC particles having different oxidation states as a result of the RTD. This is reflected in different reduction rates [93]. The average reduction rate accounting for the RTD of the solids may differ from the reduction rate calculated with the volume-averaged oxidation state. Correctly calculating the reduction rate is crucial for correctly calculating the solids species concentration at the exit of the FR and the oxidation in the AR. The FB model is modified, introducing an effectiveness that accounts for the effect of the solids RTD on the reduction reactions:

$$\varphi_{Red} = R_{si}^{ave} / R_i\left(X_i^{ave}\right) \quad (23)$$

where $R_i\left(X_i^{ave}\right)$ is the reaction rate calculated using the average conversion, and R_i^{ave} is the average reaction rate considering the solids RTD, $E(t)$:

$$R_i^{ave} = \int_0^\infty R_i(X_i(t))E(t)dt \quad (24)$$

The $X_i(t) - t$ curve is calculated using the sum of the reaction rates with the average driving force of H_2, CO and CH_4 in the emulsion phase. For example, the average driving force for the reduction of Fe_3O_4 by H_2 in the FR is calculated by:

$$C_{H_2}^{ave} = \frac{1}{H}\int_0^H \left(C_{H_2}^e - \frac{C_{H_2O}^e}{K_{eq,r5}}\right)dz \quad (25)$$

The static head is considered the only source of pressure drop in the

Table 5
Properties of the considered solids.

	Oxygen carrier	Catalyst
Density [kg/m^3]	2496	1980
Diameter [mm]	0.2	0.2
Composition	20% Fe_2O_3 on $MgAl_2O_4$	5% Rh on Al_2O_3
u_{mf}, [$m_g^3/m_r^2 \cdot s$]	0.045	0.036
u_t, [$m_g^3/m_r^2 \cdot s$]	2.41	2.07
u_{tr}, [$m_g^3/m_r^2 \cdot s$]	5.05	4.58

Values for u_{mf} and u_t are calculated with FR inlet gas at 1073 K, u_{tr} is calculated with air at 773 K.

BFB because of the low slip velocity. The lateral and axial temperature gradients are considered negligible as the solids mixing is very efficient while the thermal conductivity and heat capacity of the solids are high. The FR can as such be considered isothermal, and its operating temperature is calculated by the overall heat balance.

For the riser AR, a 1D heterogeneous plug flow model accounting for interfacial mass and heat transfer limitations is adopted. The reaction is considered to occur under solids surfaces conditions. Though the gas-solids heat transfer is fast, the heat release from the oxidation results in very different solids and gas temperatures, which have to be calculated separately. Because of the very high superficial gas velocity and gas-solids slip velocity, both the contribution of the static and frictional pressure drop are accounted for in the pressure drop equation [94]. The reactor model equations for the FR and AR are summarized in Table 4. The constitutive equations and the boundary conditions are listed in the Supplementary Material. Selection criteria for the key constitutive equations, e.g., interchange coefficient, are also explained in the Supplementary Material.

3.4. Primary dimensions and operation conditions of the aCLR system

It is considered that in both the AR and FR, the gas and solids are fed at the bottom and leave via the top of the reactor. In a commercial scale a-CLR unit, the fuel (a mixture of H_2O or/and CO_2, and methane) fed to the FR and the air fed to the AR are preheated using the high-temperature syngas/depleted air to optimize heat recovery. In the simulation, the feed temperature to both the AR and FR is 773 K, which is a feasible temperature [56]. The properties of the two types of solids considered are listed in Table 5.

The fuel reactor is operated in the bubbling regime, with the superficial gas velocity being higher than the minimum fluidization velocity of the heavier particle, $u_{mf,1}$. Because all the reactions involving CH_4 produce two more molecules, the superficial gas velocity increases during methane conversion. On the other hand, to avoid too strong entrainment, the superficial gas velocity near the top of the bed should not be too high to avoid reaching the terminal velocity of the lighter particle, $u_{t,2}$. The feed of the FR being primarily CH_4 (mixed with a small amount of H_2O and/or CO_2), the superficial gas velocity at the exit of the FR can be roughly estimated as 3 times that at the inlet. Thus:

$$u_{mf,1} < u_{sg}^{inFR} < \frac{u_{t,2}}{3} \tag{26}$$

The design of the FR considers the capacity equivalent to 50 conventional reforming tubes with more than 95% CH_4 conversion and with a feed steam-to-methane ratio of 1/6. Following the initial simulations, a 4 m diameter, 0.8 m high (dense zone) FR is chosen. The influence of the bed height on the reactor performance will be discussed later. The air reactor is operated in riser mode. Thus, the superficial gas velocity of the air reactor should be significantly higher than the transport velocity at which massive solids circulating starts. The transport velocity is calculated by [95]:

$$Re_{tr} = u_{tr} d_p \rho_g / \mu = 2.28 Ar^{0.419} \tag{27}$$

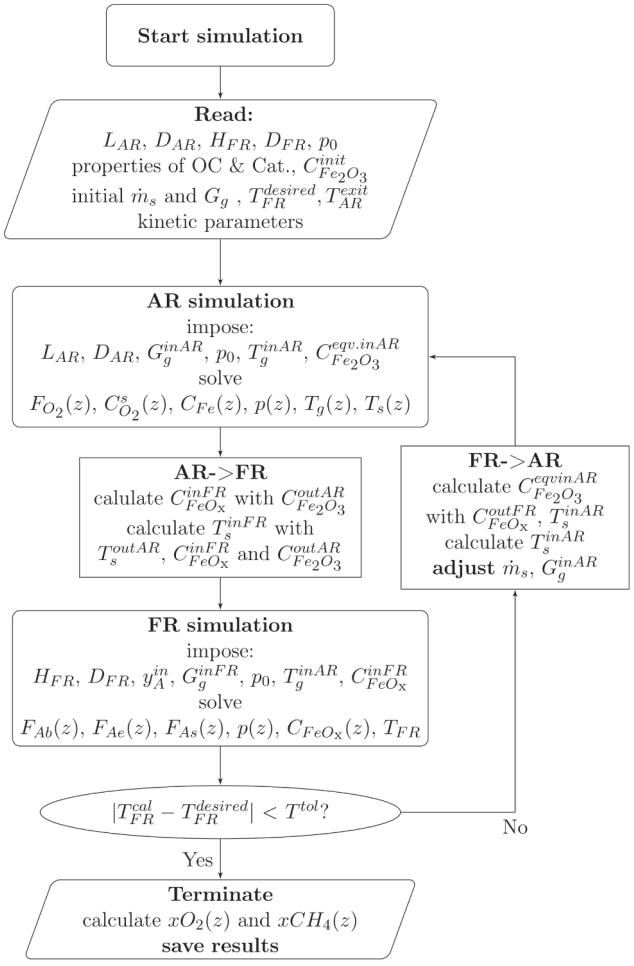

Fig. 4. Numerical solution algorithm.

$$Ar = d_p^3 \rho_g g (\rho_s - \rho_g) / \mu^2 \tag{28}$$

The diameter of the AR, d_{AR}, is determined by:

$$4G_g / \left(0.25\pi d_{AR}^2 \rho_{air}\left(T_g^{inAR}\right)\right) = 2u_{tr} \tag{29}$$

where the superficial air inlet velocity is two times the transport velocity of the OC. The air feed rate, G_g, in [kg/s] is chosen according to an oxygen-to-CH_4 ratio of around 1.2 for autothermal operation of the aCLR [22,56]. This ratio will be further adjusted to ensure autothermal operation. These considerations result in a riser diameter of 1.2 m. A riser height of 10 m was chosen to provide sufficient height to install cyclones, loop seal, etc. This height is more than needed for nearly 100% O_2 conversion with the given oxidation kinetics. Nevertheless, the riser AR is much shorter than a typical FCC riser [96].

3.5. Simulation procedure

To ensure the autothermal operation at the desired operating temperature of the FR while meeting the temperature limit of the AR, two parameters are adjusted: the air feed rate and the solids circulation rate, that is, between the AR and FR. The air feed rate is adjusted to meet the FR temperature while the solids circulation rate is adjusted to meet the AR temperature. The procedure is shown in Fig. 4.

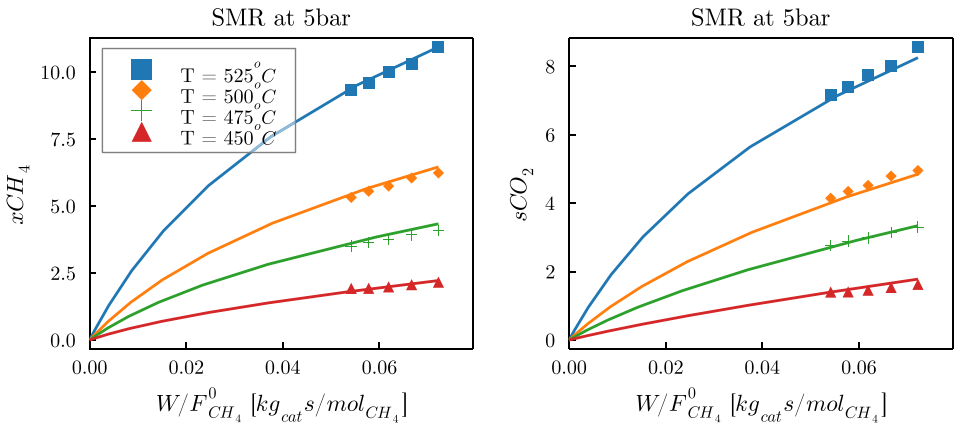

Fig. 5. Methane conversion (left) and selectivity to CO_2 (right) as a function of space time (flow rate varied) in SMR tests for P = 5 bar, S/C = 3.06, H_2/CH_4 = 1.2 and for different temperatures. Dots: experimental data; Lines: model predictions.

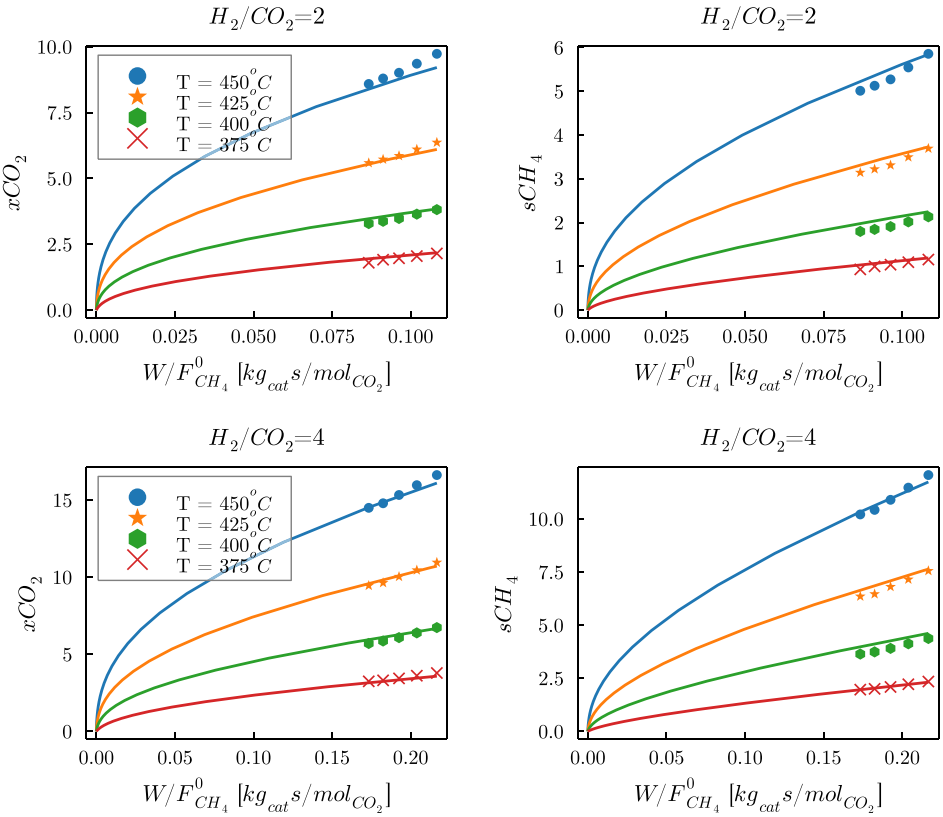

Fig. 6. Conversion into methane (left) and CO_2 conversion (right) as a function of space time (flow rate varied) in methanation tests for P = 5 bar, Ar/H_2 = 6 and for different temperatures. Dots: experimental data; Lines: model predictions.

4. Results and discussion

4.1. Experimental results and reaction kinetics

After preliminary experiments, 15.6 mg of the catalyst was used for kinetics tests to allow sufficient conversion to determine kinetics while avoiding a too high conversion to prevent temperature gradients or approaching equilibrium. The experimental data of the CH_4 conversion, xCH_4, and selectivity to CO_2, sCO_2, versus the space–time W/F^0_{CH4} during SMR experiments are shown in Fig. 5, while the experimental results of the CO_2 conversion xCO_2 selectivity to CH_4, sCH_4, versus the space–time W/F^0_{CH4} during methanation and RWGS experiments are shown in Fig. 6.

The data at each temperature were separately treated using linear least squares regression to obtain rate constants and adsorption equilibrium constants at each temperature. The estimates per temperature are shown in Table S5 in the Supplementary Material. It should be noted that the estimation of the statistically significant value of k_2 from SMR experimental data is usually challenging because reaction (r2) approaches equilibrium in the window of tested SMR operating conditions and the partial pressure of CO and CO_2 are very low [12,58]. The WGS rate parameters were therefore estimated from the methanation and RWGS data only. In addition, because of the low CO partial pressure in SMR experiments, K_{CO} is only estimated using WGS data, while for a similar reason, K_{CH4} and K_{H2O} are only estimated using SMR data. Following isothermal data treatment, all obtained data at different temperatures were used jointly for parameter estimation, using non-

Table 6
Parameter estimation using non-linear regression.

Parameter	Unit	Values with 95% C.I.
$A(k_{r1})$ (T_{m2})	[mol/kg_{cat}·s·$bar^{0.5}$]	48.3 ± 4.4
E_{ai}	[kJ/mol]	232.9 ± 5.1
$A(k_{r2})$ (T_{m1})	[mol/kg_{cat}·s·bar]	1438 ± 100
E_{aii}	[kJ/mol]	40.8 ± 3.7
$A(k_{r3})$ (T_{m2})	[mol/kg_{cat}·s·$bar^{0.5}$]	39.65 ± 0.37
E_{aiii}	[kJ/mol]	297.0 ± 5.2
$A(K_{H2})$ (T_{m2})	[bar^{-1}]	0.034 ± 0.0093
ΔH_{H2}	[kJ/mol]	−149.6 ± 6.0
$A(K_{CO})$ (T_{m1})	[bar^{-1}]	1759.0 ± 53.0
ΔH_{CO}	[kJ/mol]	−47.6 ± 1.9
$A(K_{CH4})$ (T_{m2})	[bar^{-1}]	0.91 ± 0.41
ΔH_{CH4}	[kJ/mol]	−42.0 ± 65.0
$A(K_{H2O})$ (T_{m2})	[bar]	5.34 ± 0.21
ΔH_{H2O}	[kJ/mol]	84.5 ± 32

linear least squares regression. The parameters estimated through linear regression were plotted using Arrhenius and van't Hoff relations to obtain the initial guesses for the activation energies and the adsorption enthalpies. This step also facilitates verifying the absence of transport limitations. To improve the convergence and reduce the impact of a pronounced correlation between the pre-exponential factor and activation energies or adsorption enthalpies, the rate and adsorption equilibrium constants were re-parameterized according to the following equation:

$$k_i = A(k_i)\exp\left(-\frac{E_{ai}}{RT}\right) = k_{i,T_m}\exp\left\{-\frac{E_{ai}}{R}\left(\frac{1}{T}-\frac{1}{T_m}\right)\right\} \tag{30}$$

$$K_A = A(K_A)\exp\left(-\frac{\Delta H_{ai}}{RT}\right) = K_{A,T_m}\exp\left\{-\frac{\Delta H_{ai}}{R}\left(\frac{1}{T}-\frac{1}{T_m}\right)\right\} \tag{31}$$

The mean temperature for the methanation and RWGS tests is $T_{m1} = 710\ K$ and for the SMR test $T_{m2} = 773\ K$. The comparison between the linear regression and non-linear regression is shown in Figure S3 in the Supplementary Material. The estimated parameters are given in Table 6, accompanied by 95% confidence intervals. The comparison between experimental data and model prediction is shown in Fig. 5 and Fig. 6 and shows a good fit. It shou be noted that the Rh-based catalyst is about 20–200 times more active than that of the traditional Ni-based catalyst for the second SMR reaction, while it has a similar activity for the first SMR reaction and is 10–100 times less active for the WGS reaction. A comparison is shown in Figure S4 in the Supplementary Material.

4.2. Commercial scale CE-aCLR unit

The methane conversion in the FR has the same definition as in section 2, while the oxygen and Fe conversion in the AR are respectively defined as:

$$xO_2(z) = 1 - F_{O_2}(z)/F^0_{O_2} \tag{32}$$

$$xFe(z) = 1 - C_{Fe}/2C^{fullOx}_{Fe_2O_3} \tag{33}$$

Approach-to-equilibrium is defined in (Eq. (34)) [28] and is calculated at the temperature of the FR using both the species concentrations on the catalysts surface and the species concentrations in the emulsion gas.

$$V_i = \frac{1}{K_{eq,i}}\prod p_j^{vj} \tag{34}$$

where *i* denotes *r1, r2* or *r3*, *j* denotes the species involved in *i*th reaction and *vj* is the stoichiometric coefficient of component *j* in reaction *i*. When V_i is below 1 the reaction proceeds to the right and vice versa. The independent simulation of the FR or AR is not very meaningful to evaluate the performance of aCLR system because:

1. Oxygen is typically fully consumed in the AR.
2. The OC is generally not fully reduced in the FR and the different oxidation state of OC affects the gas composition at the FR outlet.
3. The solids species concentrations in the FR and solids circulating rate determine the AR outlet composition.

Thus, all the presented CE-aCLR simulations results are for the coupled AR-FR system. The reactor dimensions and the operating conditions for the reference case are summarized in Table 7.

Fig. 7 shows the axial conversion and temperature profiles in the AR. Oxygen is almost fully consumed in the initial 4 m of the riser. Because the oxidation rate can be higher than the experimentally measured, the riser is sufficiently long for fully utilizing the fed oxygen. The mean Fe conversion increased from ~ 0.38 to ~ 0.79 and the temperature of the OC increased from 1073 K to 1375 K with a solids circulating rate of 55.6 kg/s. This corresponds to 49 [kg/m^2·s] that is a moderate value. Based on the solids state transition assumption, when the Fe conversion is between 2/3 and 8/9, the Fe in OC becomes a mixture of FeO and Fe_3O_4. Note that the temperature at the exit of the AR is intendedly controlled by adjusting the solids circulating rate. The AR exit

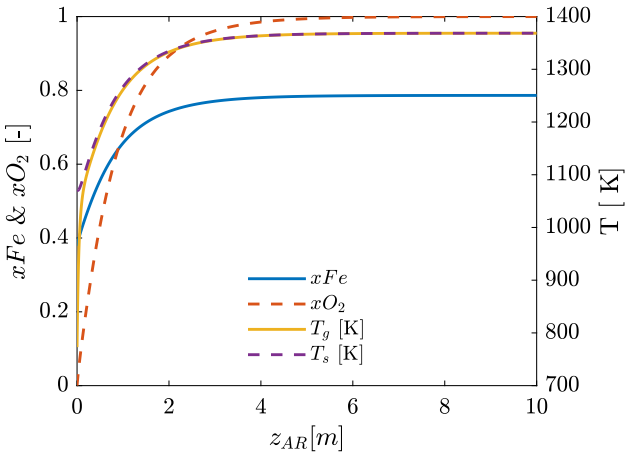

Fig. 7. Axial profile of Fe and O_2 conversion, gas and solids temperature in the AR. T_{FR} = 1073 K, $\dot{m}_s$ = 55.6 kg/s, $C^{in\ AR,\ eqv}_{Fe_2O_3}$ = 0.474 mol/kg, $C^{out\ AR,\ eqv}_{Fe_2O_3}$ = 0.983 mol/kg.

Table 7
Reactor dimensions, operation conditions, and flow streams at the inlet and outlet of the FR and AR for the reference case.

Dimensions	$D_{FR}[m]$	$H_{FR}[m]$	$D_{AR}[m]$	$H_{AR}[m]$	p_0 [bar]	T^{in}_g [K]	
	4	0.8	1.2	10	1.1	773	
FR	F_{CH4}	F_{H2O}	F_{CO}	F_{CO2}	F_{H2}	$C^{eqv}_{Fe_2O_3}$	T_s [K]
In FR	71.4	12.0	0.1	0.1	0.1	0.98	1371
Exit FR	2.3	17.9	60.83	8.53	132.4	0.474	1073
AR	$F^{inAR}_{O_2}$	F_{N_2}	$F^{outAR}_{O_2}$	$\dot{m}_s$	T^{sin}_{AR}	T^{exit}_{AR}	p_0 [bar]
	41.8	157.3	2E-3	55.6	1072	1364	1.1

All flow rates, F_A, are in [*mol/s*], $C^{eqv}_{Fe_2O_3}$ is in [*mol/kg*], $\dot{m}_s$ is in [*kg/s*], temperatures are in [K], T^{in}_g = 773 K.

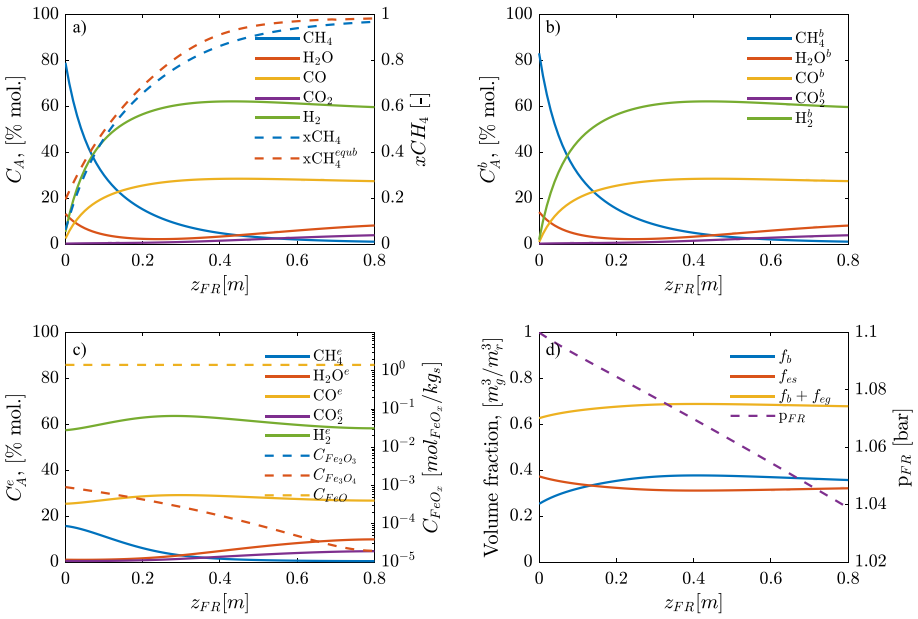

Fig. 8. Axial profiles of the (a) means species fractions and methane conversion, (b) species fractions in the bubble phase, (c) species fractions in the emulsion gas and (d) bubble, solids voidage fractions and pressure profile in the FR. Simulation of the ref. case. T_{FR} = 1073 K, feed S/C = 1/6, $\dot{m}_s$ = 55.6 kg/s.

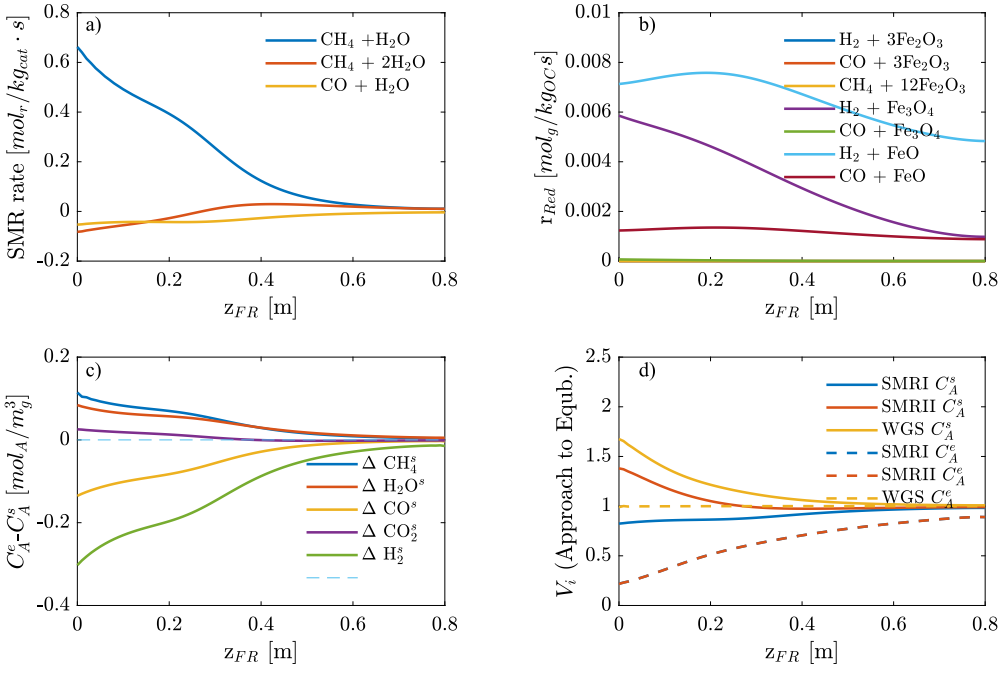

Fig. 9. Axial profiles of the: (a) SMR reaction rates, (b) reduction reaction rates, (c) concentration differences between the emulsion gas and gas on catalyst surface, (d) approach-to-equilibrium in the emulsion gas and gas in the catalyst in the FR. Simulation of ref. case, T_{FR} = 1073 K, feed S/C = 1/6.

temperature, ~1100 °C is feasible at ambient pressure but already a high value with the existing materials. The oxygen transport capacity is about 1.54 mol_O/kg_{OC}, or 0.024 kg_O/kg_{OC}, resulting in a temperature difference between the AR and the FR of ~ 300 K. The oxygen transport capacity is a relatively small value that is lower than that of the Fe_2O_3-Fe_3O_4 cycle [17]. However, the oxygen transport capacity is limited by the temperature limits instead of the intrinsic capacity, indicating that the oxygen transport capability is generally not to be concerned with metal-oxide-based OCs. Decreasing the temperature at the exit of the AR can be achieved by increasing the solids circulation rate, at the expense of a higher pressure drop in the riser. The imposed temperature limit is an operational issue relevant to various factors, e.g, the construction material, potential deactivation of OC and catalyst, and eventual heat losses, issues that will not be further addressed in this work.

The axial profiles of the mean, bubble phase, emulsion phase species concentration profiles, and of the gas and solids fractions in the FR are shown in Fig. 8. The axial profiles of the reaction rates, concentration differences between emulsion gas and gas in the catalyst, and the approach-to-equilibrium are shown Fig. 9.

Fig. 8a shows that the mean fraction of the steam decreases in the initial 0.3 m of the FR and then increases, while the mean fractions of H_2 and CO increase fast in the initial 0.2 m and then slightly decrease. This

indicates that steam methane reforming reactions are faster in the lower part of the reactor, due to high CH_4 concentration, leading to a net production of H_2 and CO. In the upper part of the reactor, the lower CH_4 concentration results in a lower driving force for mass transfer from the bubble to the emulsion phase. This slows down the SMR reactions and decreases the methane fraction in the emulsion phase. On the other hand, the reduction rate of the Fe-oxides is relatively stable (Fig. 9b), leading to a net consumption of H_2 and CO. Fig. 8a also shows the methane conversion and the equilibrium conversion calculated with the mean concentration in the FR. Both xCH_4 and xCH_4^{equb} increase with height because more oxygen is transferred from the OC to the gas. At Z_{FR} of ~ 0.2 m, the methane conversion is very close to the equilibrium conversion, indicating lack of oxygen in the gas phase. Fig. 8b shows that the species fractions in the bubble phase are very close to the mean species fractions (Fig. 8a) because a significant portion of the gas is in the bubble phase. With the relatively high superficial gas velocity, $u_{sg}^0 = 0.539$ [m_g^3/m_r^2 s], and relatively low minimum fluidization velocity of the OC, $u_{mf}^{OC} = 0.0446$ [m_g^3/m_r^2 s], the initial bubble fraction, f_b^0, is about 0.25 and the gas flux to the bubble phase is 0.5055 [m_g^3/m_r^2 s], meaning more than 90% of the gas is in the bubble phase at the FR inlet. Although the superficial gas velocity is high, the bubbling fluidized bed model is valid. As pointed by Leckner [97], even when operating in a regime that is traditionally classified as turbulent or fast fluidization, a bottom bubbling bed exists in the industrial scale fluidized bed as long as solids are sufficiently supplied. Fig. 8c shows that the species fractions in the emulsion gas are very different from those in the bubble phase near the inlet of the FR, indicating pronounced mass transfer resistance between the bubble and emulsion phase. It is seen in Fig. 8c that the mean concentration of Fe_3O_4 is very low while that of FeO is relatively high. However, as the reduction of Fe_3O_4 is faster, the volume-averaged reduction rates of Fe_3O_4 and FeO are comparable, as seen in Fig. 9b. The concentration of FeO is almost constant in the FR because of the strong axial dispersion and production of FeO from the reduction of Fe_3O_4, but the Fe_3O_4 mean concentration, although very low, is far from constant due to the very fast reduction rate. Fig. 8d shows the voidage is between 0.6 and 0.65, a typical voidage in a large-scale bubbling bed with group B particles in the same superficial gas velocity range [97].

As seen in Fig. 9a, the first SMR reaction proceeds to the right-hand side while both the WGS and the second SMR reactions proceed to the left-hand side due to the very low H_2O concentration on the catalyst surface. This indicates the SMR reactions are limited by the low concentration of H_2O. Fig. 9b shows the overall reduction rate of gaseous reactants is about 0.014 [$mol/kg_{OC}{\cdot}s$], and the reduction by H_2 is about five times faster than that by CO, reflecting the concentration difference between these two gases and different kinetics. Fig. 9c shows that the concentration difference of H_2O between the emulsion gas and gas in the catalyst is about 0.08 [mol/m_g^3], with the concentration of H_2O in the emulsion gas as low as ~ 0.12 [mol/m_g^3]. This significant difference in H_2O concentration indicates again that low H_2O concentration in the emulsion gas limits the SMR reactions. On the other hand, the SMR reaction rate is seen to be 50–100 times higher than the reduction rate, implying a 50–100 times lower concentration difference (of H_2 and CO) between the emulsion gas and the OC particles than between the emulsion gas and the catalyst particles. This justifies neglecting the mass transfer resistance for the reduction reactions. Interestingly, the concentration of CO_2 is higher in the emulsion phase than on the catalyst surface, confirming CO_2 is essentially a reactant. Different gas-phase concentrations result in different driving forces for the reactions. It is seen in Fig. 9d that V_{WGS}^e is close to unity, as WGS is expected to be close equilibrium at high temperature. V_{SMRI}^e and V_{SMRII}^e calculated with the emulsion gas concentrations, are below 1. Note that two values are very close and that only two of these equilibria are independent. On the catalyst surface, V_{SMRI}^s is below 1 while both V_{SMRII}^s and V_{WGS}^s are greater than 1. This indicates again a lack of H_2O, the result of a very low steam-to-methane feed ratio (1/6) in CE-aCLR compared to ~ 3 in SMR, and

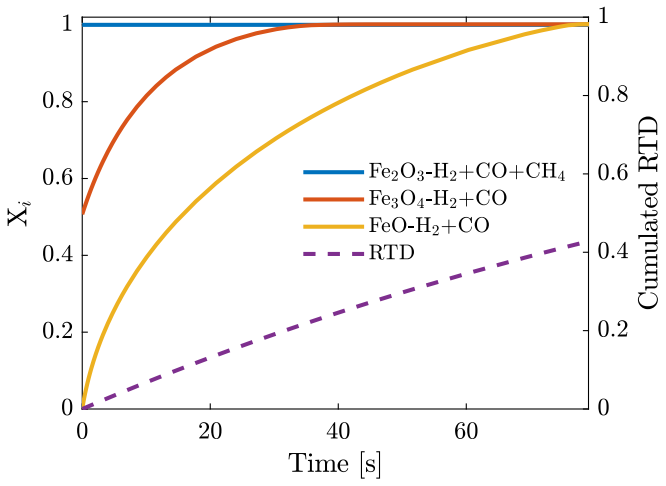

Fig. 10. The reduction conversion vs. t curve using the mean driving force and the cumulated residence time distribution of solids in the FR, $H_{FR} = 0.8$ m.

the relatively low reduction rates. The latter is due to less than 40% of the OC in the FR participating in the reduction and less than 20% of the OC containing Fe_3O_4, as seen in Fig. 10. Fig. 9d shows that, on the solids surface, all the SMR reactions approach equilibrium near the outlet of the FR, but this is not the case in the emulsion gas, the result of mass transfer resistance between the emulsion gas and the catalyst surface. But the concentration differences between the emulsion gas and gas on the catalyst surface are very small at the FR outlet, as shown in Fig. 9c. Fig. 8b shows that the concentration of CH_4 in the bubble phase is low at the FR outlet and close to the CH_4 concentration in the emulsion gas.

The inlet and outlet flow streams are summarized in Table 7. The yield to syngas ($H_2 + CO$) per mole of converted CH_4 ratio is about 2.91, meaning nearly 97% of the converted methane is converted to syngas. The energy efficiency of CE-aCLR can be estimated by the ratio of lower heat values (LHV) of the converted CH_4 and the produced syngas, $\eta_e = LHV_{H_2+CO,exitofFR}/LHV_{CH_4,inletofFR} = 89\%$. This is competitive with conventional methane reforming processes, SMR and ATR. The outlet H_2/CO ratio is 2.17 that meets the requirement for F-T and methanol synthesis. The bed inventory of the FR per mole of CH_4 per second can be estimated by $inv_{OC} = f_s^{ave}\Omega_r H_{FR}\alpha_{OC}\rho_{OC}/F_{CH4}$ and $inv_{cat} = f_s^{ave}\Omega_r H_{FR}\alpha_{cat}\rho_{cat}/F_{CH4}$. For the reference case, the parameters and properties are shown

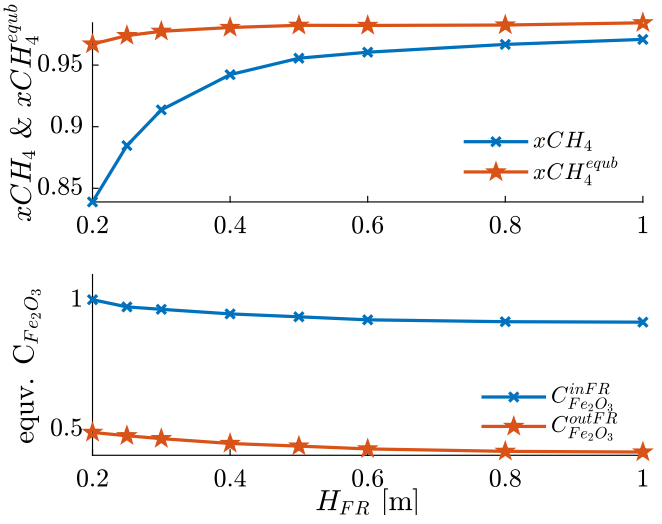

Fig. 11. (Top) methane conversion vs. FR height, (Bottom) equivalent Fe_2O_3 concentration at the inlet and outlet of the FR vs. FR height. $T_{FR} = 1073$ K, feed S/C = 1/6.

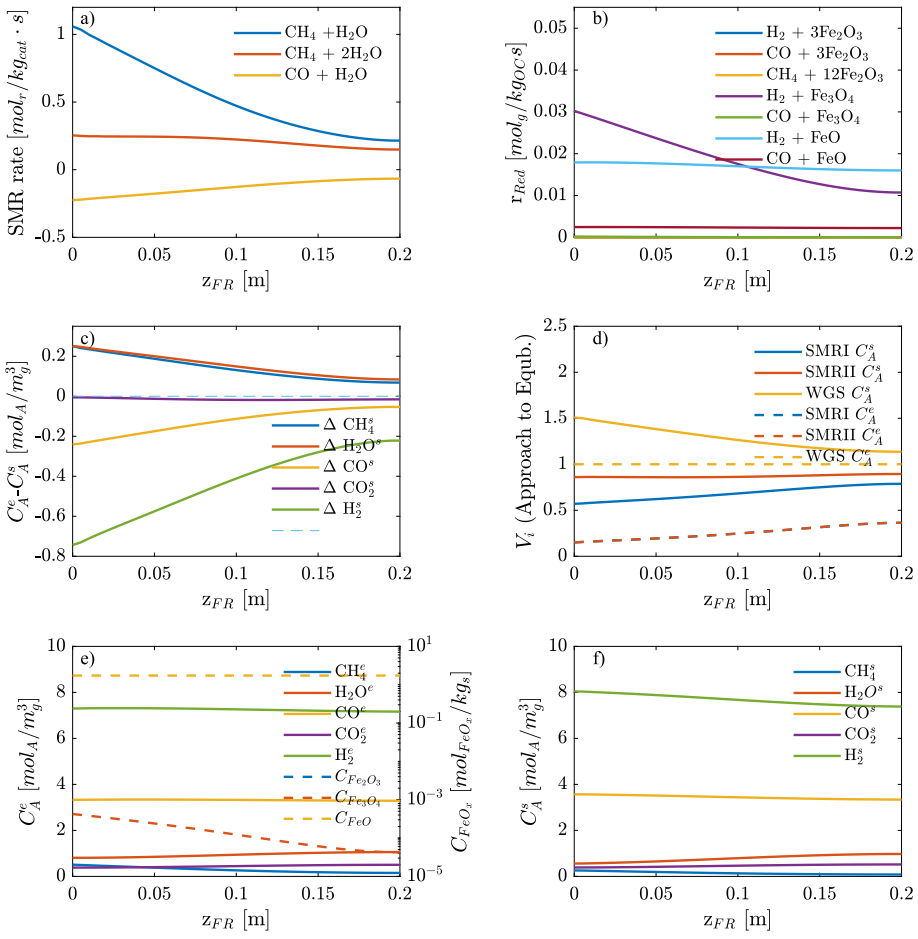

Fig. 12. Axial profiles in a 0.2 m high FR: (a) SMR reaction rates, (b) reduction reaction rates, (c) concentration differences between the emulsion gas and gas on the catalyst surface, (d) approach-to-equilibrium in emulsion gas and in the gas on the catalyst, (e) gas concentration of emulsion gas and (f) concentration of gas on the catalyst surface. T_{FR} = 1073 K, feed S/C = 1/6.

in Table 5 and Table 7. The OC inventory in the FR is inv_{OC} = $0.35*2^2*\pi*0.8*0.95*2496/71.4$ = $116.8\ kg_{OC}*s/mol_{CH4}$, while the catalyst inventory is inv_{cat} = $0.35*2^2*\pi*0.8*0.05*1980/71.4$ = $4.88\ kg_{cat}*s/mol_{CH4}$. As a comparison, a conventional packed bed SMR typically uses reactors with D_r = 0.1 m and H_r = 12 m. Thus, the catalyst inventory of a SMR with the same capacity is inv_{cat} = $0.5*0.25*0.1^2*\pi*12*50*1980/71.4 = 65.34\ kg_{cat}*s/mol_{CH4}$ (assuming a typical bed porosity of a SMR tubular reactor of 0.5, and an identical SMR catalyst). Thus, the CE-aCLR needs ca. 10 times less catalyst than conventional SMR, although it requires doubled weight of Fe-based OC. The latter is, however, typically much cheaper than SMR catalysts.

4.3. Sensitivity analysis

4.3.1. Influence of FR bed height on the performance of the CE-aCLR unit

The fluidized bed height and diameter affect the operating cost and reactor performance as it determines the catalyst and OC inventories, as well as the residence time of the gas in the bed. Fig. 11 shows the relationship between the methane conversion and the FR bed height, with xCH_4^{equb} being calculated using the exit species concentrations. Both xCH_4 and xCH_4^{equb} increase with bed height but the influence is not linear due to the strong axial mixing in the BFB. The equivalent Fe_2O_3 concentration, also shown in Fig. 11, is higher in the shallower bed, due to the shorter solids residence time in the FR. In shallower beds, the difference between xCH_4 and xCH_4^{equb} is more significant than that in a deeper bed. In shallower beds, the methane conversion is more severely limited by the mass transfer resistance between the bubble and emulsion phase, leading to a high CH_4 slip within the bubble gas. The methane

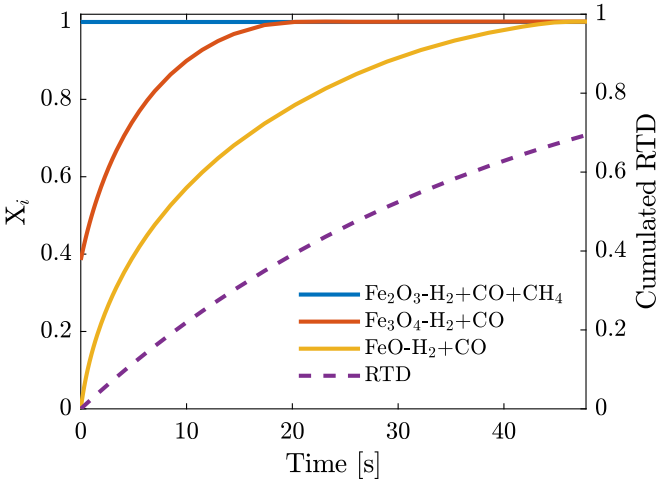

Fig. 13. The reduction conversion-t curve using the mean driving force and the cumulated residence time distribution of the solids in the FR, H_{FR} = 0.2 m.

conversion reaches approximately 0.83 with a 0.2 m high FR, while doubling the bed height (H_{FR} = 0.4 m) results in an increase of xCH_4 to 0.94. A further increase of the bed height results in a less significant increase in methane conversion. The reason is found in the species and reaction rate profiles. In deeper beds, the methane conversion is mainly constrained by chemical equilibrium. With 96% CH_4 conversion, a 0.8 m

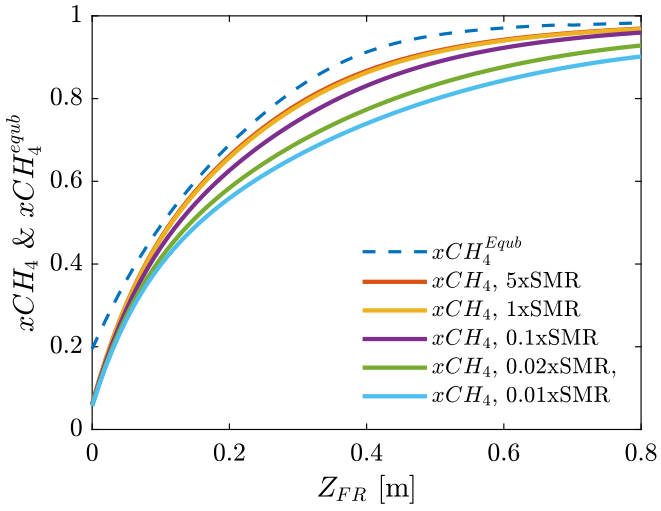

Fig. 14. Effect of catalyst activity on the methane conversion in the 0.8 m height FR.

bed height FR is chosen for further sensitivity studies.

Axial profiles of the reaction rates, approach-to-equilibrium, gas concentrations, and gas-catalyst concentration differences in the 0.2 m FR are shown in Fig. 12. As can be seen from Fig. 12a, SMR rates are significantly higher near the inlet of the FR than that in the 0.8 m high bed (Fig. 9a). This is due to the higher H_2O concentration (Fig. 12e). For the same reason, both r1 and r3 proceed to the right. The concentration differences between the emulsion gas and catalyst are much higher than that in the 0.8 m FR, as seen in Fig. 12c. As shown in Fig. 12b, the reduction rates are faster than in the 0.8 m FR, because of the higher oxidation state of the OC. In the 0.2 m-high FR approximately 60% of the OC contains Fe_3O_4 and about 90% of the OC contains FeO, as shown in Fig. 13. This is due to the shorter residence time of the OC particles in the 0.2 m FR. Although the mean Fe_3O_4 concentration is much lower than that of FeO, the reduction of Fe_3O_4 by H_2 is faster than that of FeO near the inlet of the FR, which reflects faster reduction kinetics. All the SMR reactions are far from equilibrium at the exit of the 0.2 m FR, as shown in Fig. 12d. In the 0.8 m-high FR, all the SMR reactions were very close to equilibrium under catalyst surface conditions.

4.3.2. *Influence of catalyst activity on the performance of the CE-aCLR unit*

The sensitivity of the reactor performance to the catalyst activity is of great interest because of two reasons: 1. During long-term operation,

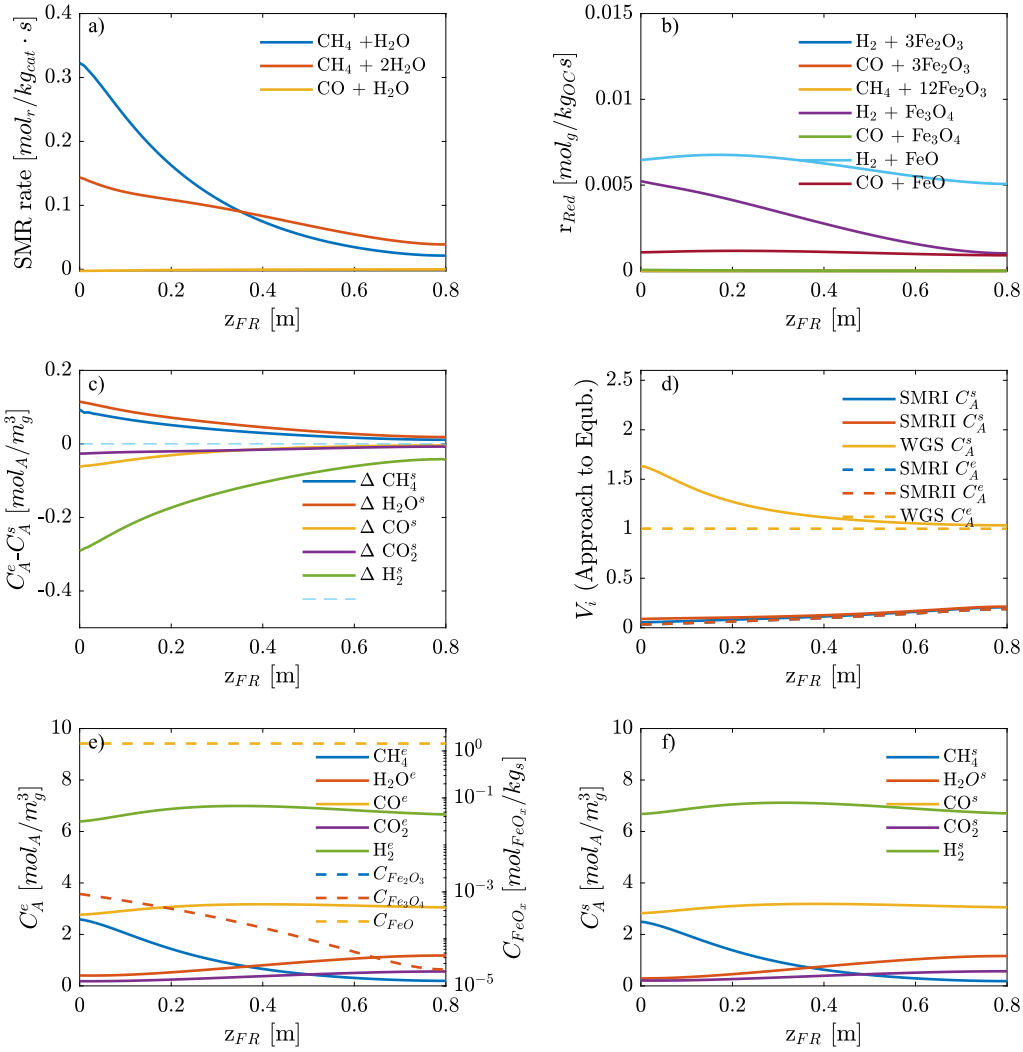

Fig. 15. Axial profiles in the FR with 0.01x reference catalyst activity: (a) SMR reaction rates, (b) reduction reaction rates, (c) concentration differences between the emulsion gas and gas on catalyst surface, (d) approach-to-equilibrium in the emulsion gas and gas in the catalyst, (e) gas concentrations of emulsion gas and (f) concentration of the gas on the catalyst surface. Simulation of ref. case, T_{FR} = 1073 K, feed S/C = 1/6.

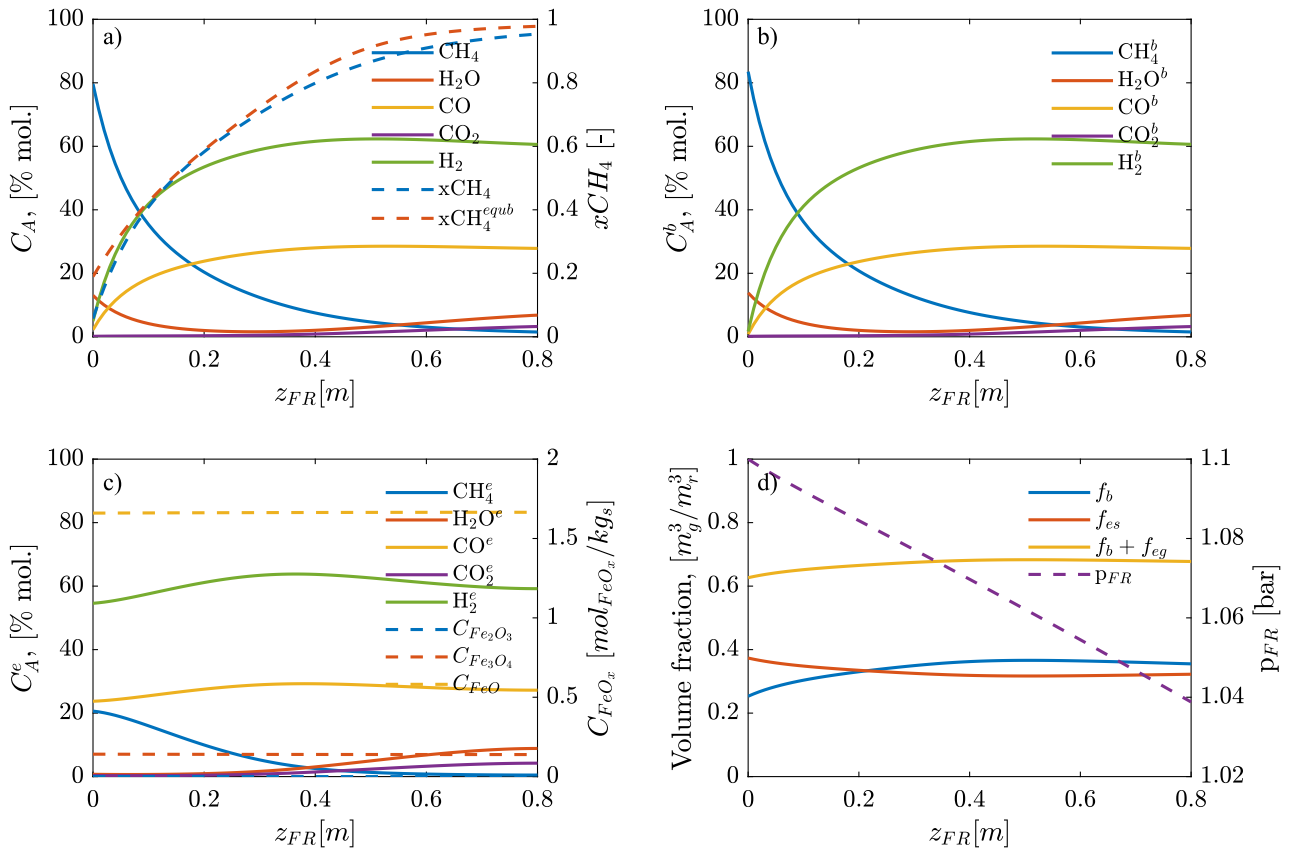

Fig. 16. Axial profiles of the (a) means species fractions and methane conversion, (b) species fractions in the bubble phase, (c) species fractions in the emulsion gas and (d) bubble, emulsion and solids fractions and pressure profile in the FR. With 0.1x reduction rate for the OC.

deactivation of catalyst is inevitable [13,98]. 2. The catalyst considered in this work is a relatively expensive Rh-based catalyst with 5% Rh, which was selected because commercially available and because of the high intrinsic activity of Rh for SMR [99]. It is of interest to know the potential of using a less active catalyst with other metals or with less metal loading.

Fig. 14 shows xCH_4 vs bed height in a 0.8 m FR with the catalyst activity ranging from 0.01 to 5 times as the reference activity. It is seen that increasing the activity of the catalyst hardly increases the methane conversion. Decreasing the activity by 10 times slightly affects the methane conversion profile but hardly the exit methane conversion. This confirms that the limiting factors are bubble-emulsion mass transfer and lack of steam. Further decreasing the catalytic activity by 50 or 100 times shows a more significant effect on the exit methane conversion.

The axial profiles of the reaction rates, species concentrations, and approach-to-equilibrium in the 0.8 m FR with an only 0.01 times active SMR catalyst are shown in Fig. 15. Although the catalytic activity is much lower, the overall SMR rate at the inlet of the FR is similar to that with the reference catalyst activity due to a higher H_2O concentration. For the same reason, both r1 and r3 proceed to the right. CO_2 is a product instead of a reactant. This implies that the overall methane conversion in the FR is still limited profoundly by transport phenomena, i.e., the mass transfer between the bubble phase and emulsion phase. As seen from Fig. 9b and Fig. 15b, the reduction reactions are not much affected by the 100 times reduced catalyst activity. Fig. 15d shows, however, that the SMR reactions are far from equilibrium at the FR outlet in contrast with what is observed with reference SMR activity (Fig. 9b). The methane concentrations in the emulsion phase and on the catalyst surface are much higher than that with the reference SMR activity, as seen from Fig. 15e and Fig. 15f. Thus, when the fraction of catalyst is around 5% wt. of the solids inventory in the FR, the catalyst should be at least

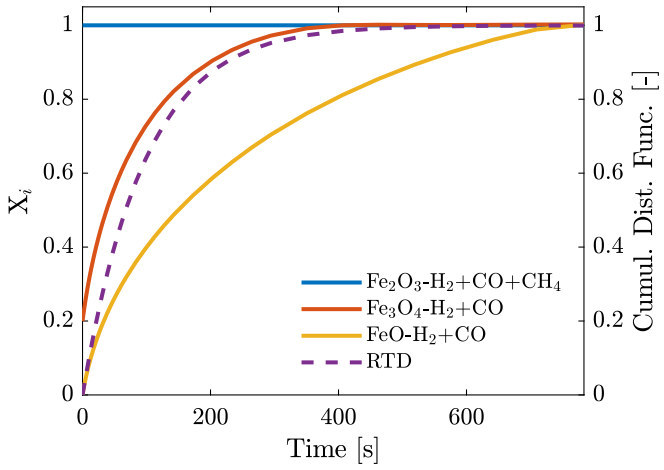

Fig. 17. The reduction conversion-t curve using the mean driving force and the cumulated residence time distribution of the solids in the FR with 0.1x reduction rate, H_{FR} = 0.8 m.

0.1 times as active as the Rh-based catalyst studied in this work.

4.3.3. Influence of OC reactivity on the performance of the CE-aCLR unit

The reduction kinetics considered in this work is for synthesized OCs that exhibit fast reduction of Fe_2O_3 to Fe typically within 100 s at 800 °C with 10% H_2. Naturally existing Fe-containing materials such as iron ore that have been studied for chemical looping processes [39,80,100] have reduction rates that are usually slower than those of the synthesized OCs. Therefore, the influence of a lower reduction rate is studied in this section. Fig. 16 shows the axial profiles in the FR with a 0.1x reduction

rate. The gas concentration profiles are almost identical to those with the reference reduction rate, while slightly higher CH_4 is observed. The difference between xCH_4 and xCH_4^{equb} is smaller than that in the reference case. This is due to lower H_2O concentration with the reduced reduction kinetics. The Fe_3O_4 and FeO mean concentrations are seen to be higher than that in the reference case, as shown in Fig. 16c. This can be explained by the oxidation state of the OC in the FR. Fig. 17 shows the conversion-time curve of the OC with the 0.1x reduction rate and the cumulated RTD of the solids. Almost all OC particles in the FR contain Fe_3O_4 and all have a FeO conversion lower than ~ 80%. In the FR with reference reduction kinetics, only 40% of the OC particles participated in the reduction. With reduced reduction kinetics, all the OC particles participate in the reduction. This explains a similar volume-averaged reduction rate with slower intrinsic reduction kinetics. In addition, this clearly illustrates that the volume-averaged reduction rates are not only related to the reduction kinetics of the OC, but also to the flow pattern properties of the reactor. In this case, the particles in the FR have a long mean residence time and long-tail RTD. Thus, using a low-cost OC, e.g., iron ore, is possible in the CE-aCLR system with a Rh-based SMR catalyst. This reduces the operation cost of the system and partially compensates for the high cost of the catalyst.

5. Conclusions

Catalyst-enhanced autothermal Chemical Looping Reforming (CE-aCLR) using a noble-metal based steam methane reforming (SMR) catalyst and a synthesized Fe-based oxygen carrier (OC) is proposed to address environmental concerns associated with Ni-based material, and the low CH_4 conversion related to the low reactivity of Fe-based OCs. The well-demonstrated aCLR configuration with a riser air reactor (AR) and a bubbling fluidized bed fuel reactor (FR), was considered when designing a commercial scale CE-aCLR unit.

Firstly, the intrinsic kinetics of an environmentally friendly Rh-based SMR catalyst is carefully studied using a well-designed micro-fixed bed reactor under experimental conditions that eliminate transport limitations and ensure isothermal operations and plug flow. To widen the temperature range for parameter estimation, both SMR and methanation and reverse of water–gas-shift experiments were carried out. Parameter estimation combines linear and non-linear regression.

The feasibility of the novel process at commercial scale is evaluated via numerical simulations using a coupled multi-scale reactor model. This model is based on a previously developed and validated aCLR model [56] that was modified to account for the distinct features of CE-aCLR. The model considers: 1. the nature of the reactor hydrodynamics, 2. mass transfer between the bubble and emulsion phases, 3. mass transfer between the gas and solid phase within the emulsion phase, 4. detailed reaction kinetics. The latter includes the derived SMR reaction kinetics for the Rh-based catalyst studied in this work, OC reduction kinetics adopted from literature, and the OC oxidation kinetics estimated from fixed bed experiments. In addition, the influence of residence time distribution of the solids in the FR on the reduction of the OC is accounted for. Dimensions for a commercial scale CE-aCLR unit are proposed and a performance study and sensitivity study are presented.

The simulation results show that a methane conversion as high as 96% and high syngas selectivity can be achieved in the commercial CE-aCLR unit with realistic reactor dimensions and solids circulation rate. The core of CE-aCLR is found to be the SMR catalyst, which should be sufficiently active to ensure high methane conversion. In contrast, the performance of the CE-aCLR unit was not very sensitive to the activity of OC. This is explained by the higher oxidation state of the OC particles in the FR when the reduction rate reduces. Even when the reduction rate of the OC reduced by a factor 10, similarly high methane conversions can be achieved. This opens perspective for using low-cost OCs, e.g., iron ore instead of the considered synthetic Fe-based OC.

CRediT authorship contribution statement

Zirui He: Conceptualization, Methodology, Investigation, Software, Formal analysis, Visualization, Writing – original draft, Writing – review & editing. **Florent Minette:** Investigation, Formal analysis. **Juray De Wilde:** Conceptualization, Methodology, Resources, Writing – review & editing, Supervision.

Declaration of Competing Interest

The authors declare that they have no known competing financial interests or personal relationships that could have appeared to influence the work reported in this paper.

Data availability

The data that has been used is confidential.

Acknowledgements

This work is supported by the Fond de la Recherche Scientifique de la Belgique (F.R.S.-FNRS) project (T.0230.16). Zirui He acknowledges the financial support from China Scholarships Council (No. 201606220058).

Appendix A. Supplementary material

Supplementary data to this article can be found online at https://doi.org/10.1016/j.enconman.2023.117525.

References

[1] IPCC. Climate Change 2022: Impacts, Adaptation and Vulnerability: Summary for Policymakers. Cambridge, UK and New York, NY, USA: Cambridge University Press; 2022.
[2] Li Y, Su M, Xie X, Wu S, Liu C. CO2 capture performance of synthetic sorbent prepared from carbide slag and aluminum nitrate hydrate by combustion synthesis. Appl Energy 2015;145:60–8. https://doi.org/10.1016/j.apenergy.2015.01.061.
[3] Bui M, Adjiman CS, Bardow A, Anthony EJ, Boston A, Brown S, et al. Carbon capture and storage (CCS): the way forward. Energ Environ Sci 2018;11(5):1062–176. https://doi.org/10.1039/C7EE02342A.
[4] Rasul MG, Hazrat M, Sattar MA, Jahirul MI, Shearer MJ. The future of hydrogen: Challenges on production, storage and applications. Energ Conver Manage 2022;272:116326. https://doi.org/10.1016/j.enconman.2022.116326.
[5] Janošovský J, Boháčiková V, Kraviarová D, Variny M. Multi-criteria decision analysis of steam reforming for hydrogen production. Energ Conver Manage 2022;263:115722. https://doi.org/10.1016/j.enconman.2022.115722.
[6] Dieterich V, Buttler A, Hanel A, Spliethoff H, Fendt S. Power-to-liquid via synthesis of methanol, DME or Fischer–Tropsch-fuels: a review. Energ Environ Sci 2020;13(10):3207–52. https://doi.org/10.1039/D0EE01187H.
[7] Chen JG, Crooks RM, Seefeldt LC, Bren KL, Bullock RM, Darensbourg MY, et al. Beyond fossil fuel-driven nitrogen transformations. Science 2018;360:6391. https://doi.org/10.1126/science.aar6611.
[8] Yan X, Li Y, Ma X, Bian Z, Zhao J, Wang Z. CeO2-modified CaO/Ca12Al14O33 bifunctional material for CO2 capture and H2 production in sorption-enhanced steam gasification of biomass. Energy 2020;192:116664. https://doi.org/10.1016/j.energy.2019.116664.
[9] Del Arnaiz PC, Cloete S. Techno-economic assessment of blue and green ammonia as energy carriers in a low-carbon future. Energ Conver Manage 2022;255:115312. https://doi.org/10.1016/j.enconman.2022.115312.
[10] IEAGHG. Techno-Economic Evaluation of SMR Based Standalone (Merchant) Hydrogen Plant with CCS; 2017.
[11] Olivos-Suarez AI, Szécsényi À, Hensen EJM, Ruiz-Martinez J, Pidko EA, Gascon J. Strategies for the Direct Catalytic Valorization of Methane Using Heterogeneous Catalysis: Challenges and Opportunities. ACS Catal 2016;6(5):2965–81. https://doi.org/10.1021/acscatal.6b00428.
[12] Xu J, Froment GF. Methane steam reforming: II. Diffusional limitations and reactor simulation. AIChE J 1989;35(1):97–103. https://doi.org/10.1002/aic.690350110.
[13] Bartholomew CH, Farrauto RJ. Fundamentals of Industrial Catalytic Processes. 2nd ed. New York, NY: John Wiley & Sons; 2011.
[14] Wu Z, Guo Z, Yang J, Wang Q. Effect of diameter distribution of particles on methane steam reforming in multi-channel grille-sphere composite packed bed. Energ Conver Manage 2022;265:115764. https://doi.org/10.1016/j.enconman.2022.115764.

[15] Yentekakis IV, Panagiotopoulou P, Artemakis G. A review of recent efforts to promote dry reforming of methane (DRM) to syngas production via bimetallic catalyst formulations. Appl Catal B 2021;296:120210. https://doi.org/10.1016/j.apcatb.2021.120210.

[16] Xiang D, Li P, Yuan X. System optimization and performance evaluation of shale gas chemical looping reforming process for efficient and clean production of methanol and hydrogen. Energ Conver Manage 2020;220:113099. https://doi.org/10.1016/j.enconman.2020.113099.

[17] Adanez J, Abad A, Garcia-Labiano F, Gayan P, de Diego LF. Progress in Chemical-Looping Combustion and Reforming technologies. Prog Energy Combust Sci 2012;38(2):215–82. https://doi.org/10.1016/j.pecs.2011.09.001.

[18] Mattisson T, Keller M, Linderholm C, Moldenhauer P, Rydén M, Leion H, et al. Chemical-looping technologies using circulating fluidized bed systems: Status of development. Fuel Process Technol 2018;172:1–12. https://doi.org/10.1016/j.fuproc.2017.11.016.

[19] Rydén M, Lyngfelt A, Mattisson T. Synthesis gas generation by chemical-looping reforming in a continuously operating laboratory reactor. Fuel 2006;85(12–13):1631–41. https://doi.org/10.1016/j.fuel.2006.02.004.

[20] de Diego LF, Ortiz M, García-Labiano F, Adánez J, Abad A, Gayán P. Hydrogen production by chemical-looping reforming in a circulating fluidized bed reactor using Ni-based oxygen carriers. J Power Sources 2009;192(1):27–34. https://doi.org/10.1016/j.jpowsour.2008.11.038.

[21] Osman M, Zaabout A, Cloete S, Amini S. Internally circulating fluidized-bed reactor for syngas production using chemical looping reforming. Chem Eng J 2019;377:120076. https://doi.org/10.1016/j.cej.2018.10.013.

[22] Pröll T, Bolhàr-Nordenkampf J, Kolbitsch P, Hofbauer H. Syngas and a separate nitrogen/argon stream via chemical looping reforming – A 140kW pilot plant study. Fuel 2010;89(6):1249–56. https://doi.org/10.1016/j.fuel.2009.09.033.

[23] Hsieh T-L, Xu D, Zhang Y, Nadgouda S, Wang D, Chung C, et al. 250 kWth high pressure pilot demonstration of the syngas chemical looping system for high purity H2 production with CO2 capture. Appl Energy 2018;230:1660–72. https://doi.org/10.1016/j.apenergy.2018.09.104.

[24] Hu J, Chen S, Xiang W. Sintering and agglomeration of Fe2O3-MgAl2O4 oxygen carriers with different Fe2O3 loadings in chemical looping processes. Fuel 2020;265:116983. https://doi.org/10.1016/j.fuel.2019.116983.

[25] Ipsakis D, Heracleous E, Silvester L, Bukur DB, Lemonidou AA. Reaction-based kinetic model for the reduction of supported NiO oxygen transfer materials by CH4. Catalysis Today Catalysis Today 2020;343:72–9. https://doi.org/10.1016/J.CATTOD.2019.01.041.

[26] Luo M, Yi Y, Wang S, Wang Z, Du M, Pan J, et al. Review of hydrogen production using chemical-looping technology. Renew Sustain Energy Rev 2018;81:3186–214. https://doi.org/10.1016/j.rser.2017.07.007.

[27] Xu T, Xu F, Moyo GG, Sun Y, Chen Z, Xiao B, et al. Comparative study of MxOy (M = Cu, Fe and Ni) supported on dolomite for syngas production via chemical looping reforming with toluene. Energ Conver Manage 2019;199:111937. https://doi.org/10.1016/j.enconman.2019.111937.

[28] Xu J, Froment GF. Methane steam reforming, methanation and water-gas shift: I Intrinsic kinetics. AIChE J 1989;35(1):88–96. https://doi.org/10.1002/aic.690350109.

[29] Bolívar Caballero JJ, Han T, Svanberg R, Zaini IN, Yang H, Gond R, et al. Advanced application of a geometry-enhanced 3D-printed catalytic reformer for syngas production. Energ Conver Manage 2023;287:117071. https://doi.org/10.1016/j.enconman.2023.117071.

[30] Cho P, Mattisson T, Lyngfelt A. Comparison of iron-, nickel-, copper- and manganese-based oxygen carriers for chemical-looping combustion. Fuel 2004;83(9):1215–25. https://doi.org/10.1016/j.fuel.2003.11.013.

[31] Ding H, Xu Y, Luo C, Wang Q, Shen C, Xu J, et al. A novel composite perovskite-based material for chemical-looping steam methane reforming to hydrogen and syngas. Energ Conver Manage 2018;171:12–9. https://doi.org/10.1016/j.enconman.2018.05.088.

[32] Tang M, Xu L, Fan M. Progress in oxygen carrier development of methane-based chemical-looping reforming: A review. Appl Energy 2015;151:143–56. https://doi.org/10.1016/j.apenergy.2015.04.017.

[33] Yu Z, Yang Y, Yang S, Zhang Q, Zhao J, Fang Y, et al. Iron-based oxygen carriers in chemical looping conversions: A review. Carbon Resources Conversion 2019;2(1):23–34. https://doi.org/10.1016/j.crcon.2018.11.004.

[34] Zhou Z, Deng G, Li L, Liu X, Sun Z, Duan L. Chemical looping co-conversion of CH4 and CO2 using Fe2O3/Al2O3 pellets as both oxygen carrier and catalyst in a fluidized bed reactor. Chem Eng J 2022;428:132133. https://doi.org/10.1016/j.cej.2021.132133.

[35] Lin Y, Zhang Z, Wang H, Fang S, Huang Z, Chen T, et al. An evaluation of the reactivity of synthetic Fe-Ni oxygen carriers: CO oxidation, H2O reforming, and toluene cracking. Energ Conver Manage 2021;240:114263. https://doi.org/10.1016/j.enconman.2021.114263.

[36] Zhang W, Zhang J, Li Q, He Y, Tang B, Li M et al. Thermodynamic Analyses of Iron Oxides Redox Reactions. In: Marquis F, editor. Proceedings of the 8th Pacific Rim International Congress on Advanced Materials and Processing. Cham: Springer International Publishing; 2016, p. 777–789.

[37] Liu Y, Qin L, Cheng Z, Goetze JW, Kong F, Fan JA, et al. Near 100% CO selectivity in nanoscaled iron-based oxygen carriers for chemical looping methane partial oxidation. Nat Commun 2019;10(1):5503. https://doi.org/10.1038/s41467-019-13560-0.

[38] Pans MA, Gayán P, de Diego LF, García-Labiano F, Abad A, Adánez J. Performance of a low-cost iron ore as an oxygen carrier for Chemical Looping Combustion of gaseous fuels. Chem Eng Res Des 2015;93:736–46. https://doi.org/10.1016/j.cherd.2014.07.001.

[39] Mendiara T, Abad A, de Diego LF, García-Labiano F, Gayán P, Adánez J. Reduction and oxidation kinetics of Tierga iron ore for Chemical Looping Combustion with diverse fuels. Chem Eng J 2019;359:37–46. https://doi.org/10.1016/j.cej.2018.11.022.

[40] Buelens LC, Galvita VV, Poelman H, Detavernier C, Marin GB. Kinetics of Multi-Step Redox Processes by Time-Resolved In Situ X-ray Diffraction. Chem Ing Tech 2016;88(11):1684–92. https://doi.org/10.1002/cite.201600057.

[41] Bohn CD, Cleeton JP, Müller CR, Davidson JF, Hayhurst AN, Scott SA, et al. The kinetics of the reduction of iron oxide by carbon monoxide mixed with carbon dioxide. AIChE J 2010:NA-NA.. https://doi.org/10.1002/aic.12084.

[42] Liu W, Lim JY, Saucedo MA, Hayhurst AN, Scott SA, Dennis JS. Kinetics of the reduction of wüstite by hydrogen and carbon monoxide for the chemical looping production of hydrogen. Chem Eng Sci 2014;120:149–66. https://doi.org/10.1016/j.ces.2014.08.010.

[43] Xu T, Jiang C, Wang X, Xiao B. Bio-oil chemical looping reforming coupled with water splitting for hydrogen and syngas coproduction: Effect of supports on the performance of Ni-Fe bimetallic oxygen carriers. Energ Conver Manage 2021;244:114512. https://doi.org/10.1016/j.enconman.2021.114512.

[44] Wei G, Huang J, Fan Y, Huang Z, Zheng A, He F, et al. Chemical looping reforming of biomass based pyrolysis gas coupling with chemical looping hydrogen by using Fe/Ni/Al oxygen carriers derived from LDH precursors. Energ Conver Manage 2019;179:304–13. https://doi.org/10.1016/j.enconman.2018.10.065.

[45] Hu J, Galvita VV, Poelman H, Detavernier C, Marin GB. Catalyst-assisted chemical looping auto-thermal dry reforming: Spatial structuring effects on process efficiency. Appl Catal B 2018;231:123–36. https://doi.org/10.1016/j.apcatb.2018.03.004.

[46] Christian Enger B, Lødeng R, Holmen A. A review of catalytic partial oxidation of methane to synthesis gas with emphasis on reaction mechanisms over transition metal catalysts. Appl Catal A 2008;346(1–2):1–27. https://doi.org/10.1016/j.apcata.2008.05.018.

[47] Lee J, Joo C, Cho H, Kim Y, Ga S, Kim J. Design of multistage fixed bed reactors for SMR hydrogen production based on the intrinsic kinetics of Ru-based catalysts. Energ Conver Manage 2022;268:115981. https://doi.org/10.1016/j.enconman.2022.115981.

[48] Yentekakis IV, Goula G, Hatzisymeon M, Betsi-Argyropoulou I, Botzolaki G, Kousi K, et al. Effect of support oxygen storage capacity on the catalytic performance of Rh nanoparticles for CO2 reforming of methane. Appl Catal B 2019;243:490–501. https://doi.org/10.1016/j.apcatb.2018.10.048.

[49] Zhao Q, Su B, Wang H, He A, He R, Kong H, et al. Mid/low-temperature solar hydrogen generation via dry reforming of methane enhanced in a membrane reactor. Energ Conver Manage 2021;240:114254. https://doi.org/10.1016/j.enconman.2021.114254.

[50] Rategarpanah A, Meshkani F, Wang Y, Arandiyan H, Rezaei M. Thermocatalytic conversion of methane to highly pure hydrogen over Ni–Cu/MgO·Al2O3 catalysts: Influence of noble metals (Pt and Pd) on the catalytic activity and stability. Energ Conver Manage 2018;166:268–80. https://doi.org/10.1016/j.enconman.2018.04.033.

[51] Snoeck J-W, Froment GF, Fowles M. Kinetic Study of the Carbon Filament Formation by Methane Cracking on a Nickel Catalyst. J Catal 1997;169(1):250–62. https://doi.org/10.1006/jcat.1997.1635.

[52] Lee Y-L, Lim D, Lee B, Upadhyay M, Brigljević B, Roh H-S, et al. Comparative Techno-economic analysis of methanol production via carbon dioxide reforming of landfill gas using a highly active and stable Nickel-based catalyst. Energ Conver Manage 2022;259:115585. https://doi.org/10.1016/j.enconman.2022.115585.

[53] Eßmann C, Weis F, Seipenbusch M, Schimmel T, Deutschmann O. Coke Formation in Steam Reforming of Natural Gas over Rhodium/Alumina Catalysts: An Atomic Force Microscopy Study using the Oscillating Friction Mode. Z Phys Chem 2011;225(11–12):1207–24. https://doi.org/10.1524/zpch.2011.0160.

[54] Sigma-Aldrich. Safety Data Sheet of Sigma-Aldrich 212857, 5% Rhodium on Alumina; Available from: https://www.sigmaaldrich.com/SG/en/sds/aldrich/212857.

[55] Alfa Aesar. Material Safety Data Sheet of Nickel Based Steam Methane Reforming Catalyst, HiFUEL R110; Available from: https://us.vwr.com/assetsvc/asset/en_US/id/8138727/contents.

[56] He Z, De Wilde J. Numerical simulation of commercial scale autothermal chemical looping reforming and bi-reforming for syngas production. Chem Eng J 2021;417:128088. https://doi.org/10.1016/j.cej.2020.128088.

[57] Froment GF, Bischoff KB, De Wilde J. Chemical Reactor Analysis and Design. Hoboken, N.J.: Wiley; 2010.

[58] Minette F, Lugo-Pimentel M, Modroukas D, Davis AW, Gill R, Castaldi MJ, et al. Intrinsic kinetics of steam methane reforming on a thin, nanostructured and adherent Ni coating. Appl Catal B 2018;238:184–97. https://doi.org/10.1016/j.apcatb.2018.07.015.

[59] Mears DE. Diagnostic criteria for heat transport limitations in fixed bed reactors. J Catal 1971;20(2):127–31. https://doi.org/10.1016/0021-9517(71)90073-X.

[60] Menon PG, de Deken JC, Froment GF. Formaldehyde as an intermediate in the steam reforming of methane. J Catal 1985;95(1):313–6. https://doi.org/10.1016/0021-9517(85)90035-1.

[61] Obradović A, Likozar B, Levec J. Steam Methane Reforming over Ni-based Pellet-type and Pt/Ni/Al2O3 Structured Plate-type Catalyst: Intrinsic Kinetics Study. Ind Eng Chem Res 2013;52(38):13597–606. https://doi.org/10.1021/ie401551m.

[62] Stewart WE, Caracotsios M. Computer-aided modeling of reactive systems. Hoboken, N.J.: Wiley-Interscience: AIChE; Chichester John Wiley [distributor]; 2008.

[63] Hosten, L., H., Froment GF. Parameter estimation in multiresponse models; 1975.

[64] Penthor S, Zerobin F, Mayer K, Pröll T, Hofbauer H. Investigation of the performance of a copper based oxygen carrier for chemical looping combustion in a 120 kW pilot plant for gaseous fuels. Appl Energy 2015;145:52–9. https://doi.org/10.1016/j.apenergy.2015.01.079.
[65] Kolbitsch P, Pröll T, Hofbauer H. Modeling of a 120kW chemical looping combustion reactor system using a Ni-based oxygen carrier. Chem Eng Sci 2009;64(1):99–108. https://doi.org/10.1016/j.ces.2008.09.014.
[66] Rowe PN, Nienow AW. Particle mixing and segregation in gas fluidised beds. A review. Powder Technol 1976;15(2):141–7. https://doi.org/10.1016/0032-5910(76)80042-3.
[67] Dahl SR, Hrenya CM. Size segregation in gas–solid fluidized beds with continuous size distributions. Chem Eng Sci 2005;60(23):6658–73. https://doi.org/10.1016/j.ces.2005.05.057.
[68] Joseph GG, Leboreiro J, Hrenya CM, Stevens AR. Experimental segregation profiles in bubbling gas-fluidized beds. AIChE J 2007;53(11):2804–13. https://doi.org/10.1002/aic.11282.
[69] Chladek J, Jayarathna CK, Moldestad BM, Tokheim L-A. Fluidized bed classification of particles of different size and density. Chem Eng Sci 2018;177:151–62. https://doi.org/10.1016/j.ces.2017.11.042.
[70] Jang HT, Park TS, Cha WS. Mixing–segregation phenomena of binary system in a fluidized bed. J Ind Eng Chem 2010;16(3):390–4. https://doi.org/10.1016/j.jiec.2009.10.003.
[71] Cano-Pleite E, Hernández-Jiménez F, Acosta-Iborra A, Tsuji T, Müller CR. Segregation of equal-sized particles of different densities in a vertically vibrated fluidized bed. Powder Technol 2017;316:101–10. https://doi.org/10.1016/j.powtec.2017.01.007.
[72] Saidi M, Basirat Tabrizi H, Chaichi S, Dehghani M. Pulsating flow effect on the segregation of binary particles in a gas–solid fluidized bed. Powder Technol 2014;264:570–6. https://doi.org/10.1016/j.powtec.2014.06.003.
[73] Liu W, Ismail M, Dunstan MT, Hu W, Zhang Z, Fennell PS, et al. Inhibiting the interaction between FeO and Al2O3 during chemical looping production of hydrogen. RSC Adv 2014;5(3):1759–71. https://doi.org/10.1039/C4RA11891J.
[74] Longo A, Theofanidis SA, Cavallari C, Srinath NV, Hu J, Poelman H, et al. What Makes Fe-Modified MgAl2O4 an Active Catalyst Support? Insight from X-ray Raman Scattering. ACS Catal 2020;10(12):6613–22. https://doi.org/10.1021/acscatal.0c00759.
[75] Zieliński J, Zglinicka I, Znak L, Kaszkur Z. Reduction of Fe2O3 with hydrogen. Appl Catal A 2010;381(1–2):191–6. https://doi.org/10.1016/j.apcata.2010.04.003.
[76] Abad A, García-Labiano F, de Diego LF, Gayán P, Adánez J. Reduction Kinetics of Cu-, Ni-, and Fe-Based Oxygen Carriers Using Syngas (CO + H2) for Chemical-Looping Combustion. Energy Fuels 2007;21(4):1843–53. https://doi.org/10.1021/ef070025k.
[77] Kathe M, Empfield A, Sandvik P, Fryer C, Zhang Y, Blair E, et al. Utilization of CO2 as a partial substitute for methane feedstock in chemical looping methane–steam redox processes for syngas production. Energ Environ Sci 2017;10(6):1345–9. https://doi.org/10.1039/C6EE03701A.
[78] Cabello A, Abad A, García-Labiano F, Gayán P, de Diego LF, Adánez J. Kinetic determination of a highly reactive impregnated Fe2O3/Al2O3 oxygen carrier for use in gas-fueled Chemical Looping Combustion. Chem Eng J 2014;258:265–80. https://doi.org/10.1016/j.cej.2014.07.083.
[79] Abad A, Adánez J, García-Labiano F, de Diego LF, Gayán P, Celaya J. Mapping of the range of operational conditions for Cu-, Fe-, and Ni-based oxygen carriers in chemical-looping combustion. Chem Eng Sci 2007;62(1–2):533–49. https://doi.org/10.1016/j.ces.2006.09.019.
[80] Monazam ER, Breault RW, Siriwardane R, Richards G, Carpenter S. Kinetics of the reduction of hematite (Fe2O3) by methane (CH4) during chemical looping combustion: A global mechanism. Chem Eng J 2013;232:478–87. https://doi.org/10.1016/j.cej.2013.07.091.
[81] Johansson M, Mattisson T, Lyngfelt A. Creating a Synergy Effect by Using Mixed Oxides of Iron- and Nickel Oxides in the Combustion of Methane in a Chemical-Looping Combustion Reactor. Energy Fuels 2006;20(6):2399–407. https://doi.org/10.1021/ef0600681.
[82] Rydén M, Cleverstam E, Johansson M, Lyngfelt A, Mattisson T. Fe2O3 on Ce-, Ca-, or Mg-stabilized ZrO2 as oxygen carrier for chemical-looping combustion using NiO as additive. AIChE J 2010;56(8). https://doi.org/10.1002/aic.12143.
[83] Bhavsar S, Veser G. Chemical looping beyond combustion: production of synthesis gas via chemical looping partial oxidation of methane. RSC Adv 2014;4(88):47254–67. https://doi.org/10.1039/C4RA06437B.
[84] Grosvenor AP, Kobe BA, McIntyre NS. Activation energies for the oxidation of iron by oxygen gas and water vapour. Surf Sci 2005;574(2–3):317–21. https://doi.org/10.1016/j.susc.2004.10.043.
[85] Grosvenor AP, Kobe BA, McIntyre NS. Examination of the oxidation of iron by oxygen using X-ray photoelectron spectroscopy and QUASESTM. Surf Sci 2004;565(2–3):151–62. https://doi.org/10.1016/j.susc.2004.06.210.
[86] de Vos Y, Vamvakeros A, Matras D, Jacobs M, van der Voort P, van Driessche I, et al. Sustainable iron-based oxygen carriers for hydrogen production – Real-time operando investigation. Int J Greenhouse Gas Control 2019;88:393–402. https://doi.org/10.1016/j.ijggc.2019.06.016.
[87] de Vos Y, Jacobs M, van der Voort P, van Driessche I, Snijkers F, an Verberckmoes. Sustainable iron-based oxygen carriers for Chemical Looping for Hydrogen Generation. Int J Hydrogen Energy 2019;44(3):1374–91. https://doi.org/10.1016/j.ijhydene.2018.11.099.
[88] Abad A, Adánez J, Cuadrat A, García-Labiano F, Gayán P, de Diego LF. Kinetics of redox reactions of ilmenite for chemical-looping combustion. Chem Eng Sci 2011;66(4):689–702. https://doi.org/10.1016/j.ces.2010.11.010.
[89] He Z, Minette F, De Wilde J. The Ultra-Fast Oxidation Rate of a Synthetic Fe-Based Oxygen Carrier: Experiment and Simulation Study. SSRN Journal 2022. https://doi.org/10.2139/ssrn.4118495.
[90] Kunii D, Levenspiel O. Fluidized reactor models. 1. For bubbling beds of fine, intermediate, and large particles. 2. For the lean phase: freeboard and fast fluidization. Ind Eng Chem Res 1990;29(7):1226–34.
[91] Kunii D, Levenspiel O. Fluidization Engineering. Elsevier; 1991.
[92] Miwa K, Muchi I, Mori S, Kato T. Behavior of bubbles in a gaseous fluidized-bed. Int Chem Eng 1972;12(1):187–94.
[93] Schnellmann MA, Donat F, Scott SA, Williams G, Dennis JS. The effect of different particle residence time distributions on the chemical looping combustion process. Appl Energy 2018;216:358–66. https://doi.org/10.1016/j.apenergy.2018.02.046.
[94] Breault RW, Mathur VK. High-velocity fluidized-bed hydrodynamic modeling. 1. Fundamental studies of pressure drop. Ind Eng Chem Res 1989;28(6):684–8. https://doi.org/10.1021/ie00090a006.
[95] Bi HT, Ellis N, Abba IA, Grace JR. A state-of-the-art review of gas–solid turbulent fluidization. Chem Eng Sci 2000;55(21):4789–825. https://doi.org/10.1016/S0009-2509(00)00107-X.
[96] Derouin C, Nevicato D, Forissier M, Wild G, Bernard J-R. Hydrodynamics of Riser Units and Their Impact on FCC Operation. Ind Eng Chem Res 1997;36(11):4504–15. https://doi.org/10.1021/ie970432r.
[97] Leckner B. Regimes of large-scale fluidized beds for solid fuel conversion. Powder Technol 2017;308:362–7. https://doi.org/10.1016/j.powtec.2016.11.070.
[98] Ligthart D, van Santen RA, Hensen E. Influence of particle size on the activity and stability in steam methane reforming of supported Rh nanoparticles. J Catal 2011;280(2):206–20. https://doi.org/10.1016/j.jcat.2011.03.015.
[99] Jones G, Jackobsen JG, Shim SS, Kleis J, Andersson MP, Rossmeisl J, et al. First principles calculations and experimental insight into methane steam reforming over transition metal catalysts. J Catal 2008;259(1):147–60. https://doi.org/10.1016/j.jcat.2008.08.003.
[100] Tan Y, Ridha FN, Duchesne MA, Lu DY, Hughes RW. Reduction Kinetics of Ilmenite Ore as an Oxygen Carrier for Pressurized Chemical Looping Combustion of Methane. Energy Fuels 2017;31(7):7598–605. https://doi.org/10.1021/acs.energyfuels.7b01038.